

Contents — Q through R

Valles Marineris Landslides: Morphologies, Ages and Dynamics <i>C. Quantin, P. Allemand, and C. Delacourt</i>	3053
The Effect of Convective Adjustment on the Global Circulation of Mars as Simulated by a General Circulation Model <i>S. C. R. Rafkin</i>	3059
Modified Impact Craters — Clues to Martian Geological Processes <i>J. Raitala, M. Aittola, V.-P. Kostama, H. Lahtela, and T. Öhman</i>	3016
Evidence for Mars Regolith Preserved in Shergottite EET79001: Differential Comminution and Chemical Weathering Records <i>M. N. Rao and D. S. McKay</i>	3130
Electrical Discharges in the Martian Dust Devils and Dust Storms <i>N. O. Renno, A. S. Wong, and S. K. Atreya</i>	3191
The Planetary Underground Tool (PLUTO) Experiment on the Beagle 2 Mars Lander <i>L. Richter, V. V. Gromov, H. Kochan, K. Kosacki, and T. Tokano</i>	3180
Viking Lander 1 and 2 Revisited: The Characterisation and Detection of Martian Dust Devils <i>T. J. Ringrose, M. C. Towner, and J. C. Zarnecki</i>	3017
Basaltic Andesite or Weathered Basalt: A New Assessment <i>S. W. Ruff</i>	3258
Evolution of Volatile-rich Crater Interior Deposits on Mars <i>P. S. Russell, J. W. Head, and M. H. Hecht</i>	3256

VALLES MARINERIS LANDSLIDES : MORPHOLOGIES, AGES AND DYNAMICS.

C. Quantin, P. Allemand, C. Delacourt, Laboratoire de Sciences de la Terre, UMR 5570 (UBC Lyon1, CNRS, ENS-Lyon), Bat Géode, 2 rue Raphael Dubois, 69622 VILLEURBANNE, France, cathy.quantin@univ-lyon1.fr.

Introduction: Valles Marineris (V.M) is affected by about 50 landslides. From Viking orbiters images, they were initially interpreted as large debris flows occurring during a unique activity period in the early history of Valles Marineris [1,2]. In contrast to this interpretation involving water intervention, a second study has found analogies between Valles Marineris landslides and dry terrestrial rock avalanches [3]. The role of fluids in the martian landslide dynamic is not unanimously admitted yet. A systematic analysis of geometry, morphology and chronology of the landslides is the key parameter to precise their dynamic. We then present results of a multidisciplinary study of Valles Marineris landslides using images with different spatial resolutions (Viking, MOC and THEMIS), Altimetric Data (MOLA) and dating methods.

Characteristics of Valles Marineris landslides:

The dimensions of landslides measured with MOLA data are one order in magnitude larger than terrestrial ones (average size is 36 x 32 km). The mass movement mobilizes the whole hillslope in opposition with the terrestrial landslides which often affect only a part of the wallslope. The thickness of the landslide deposits decreases onward from about 2 km at the foot of the scarp to 100 m at the front of the landslide.

Morphology : 46 landslides have been classified in three morphologic types from the geometry of the landslide deposit : (1) chaotic, (2) structured deposit without debris aprons and (3) structured deposit with debris aprons. The chaotic type displays a rough deposit without well identified tectonic structures (Fig.1). The structured deposit without debris aprons have tectonic structures at the back of the deposit whereas the front displays unorganised roughness (Fig.2). The structured landslides with debris aprons also show well identified extensive structures at the back of the deposit whereas the main part of the deposit is constituted by large debris aprons (Fig.3). These aprons are 200 m thick with a lobated shape. On a corresponding DEM (Fig.4.), a zone of increasing thick material at the toe of the apron is identified implying fluidization mechanisms [4]. At the toe of this kind of landslide, there are mostly several debris aprons corresponding possibly with different pulses during sliding events [1,2]. On the available M.O.C. images, all debris aprons show longitudinal ridges resulting from mechanisms of sliding at high velocity [2,5]. Then, within Valles Marineris and sometimes within a same deposit it coexists brit-

tle structures suggesting sliding mechanisms and debris aprons suggesting fluidization mechanisms.

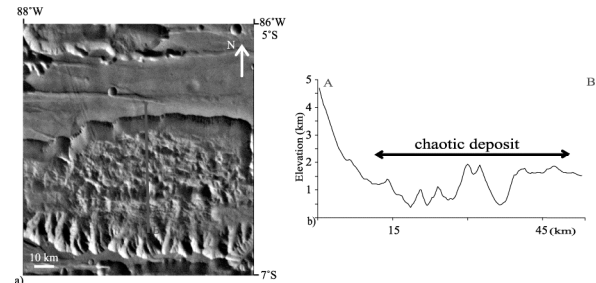


Fig.1. Chaotic type : a) Viking context, b) Topographic profile (MOLA).

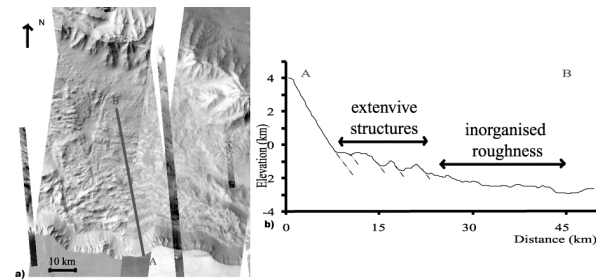


Fig.2. Structured deposit without debris aprons type a) Part of MOC and THEMIS images mosaic, b) Topographic profile (MOLA).

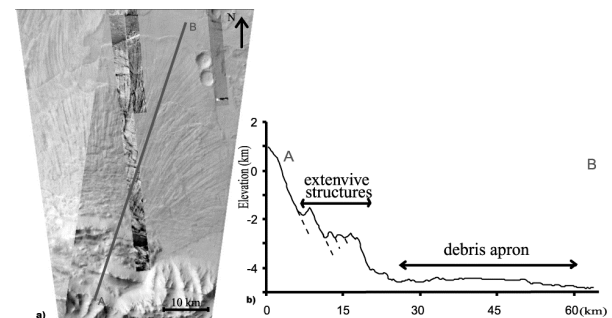


Fig.3. Structured deposit with debris aprons type a) Part of MOC and THEMIS images mosaic, b) Topographic profile (MOLA).

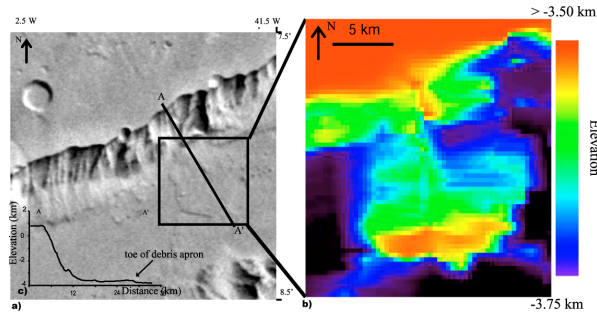


Fig.4.: Debris aprons topography a) Viking context, b) Digital Elevation Model (MOLA), c) Topographic profile.

A spatial analysis of the repartition of the morphologic types reveals that the chaotic landslides are mainly located within narrow canyons like Ius Chasma and in the enclosed Hebes Chasma. The type with debris aprons takes place essentially in the widest canyons of Valles Marineris (Gangis Chasma and on the walls of the central parts of V.M.). The distribution of the landslides type seems to be organized according to the width of the canyon where they are located.

Mobilities : The mobility of landslides is measured by the ratio between the vertical drop and the runout of the landslide. This ratio is directly related to the coefficient of friction of the material [6]. The mobility of the martian landslides ranges from 1.8 to 12.7. These large mobilities are also supported by the low deposit slopes of Valles Marineris landslides which are lower than 5° . Long run-out and low deposit slopes involve a fluidization mechanism or a basal decollement layer. Recent numerical simulations trying to explain the long run-out of Martian landslides, indicate that nor Bingham rheology, nor acoustic fluidization and not even a frictional rheology correspond to Martian landslides [7].

Volume balances : In 2D, the overlap of the profile with and without landslide shows two types of volume on both sides of the profile crossing : the eroded volume (EV) for the part before the crossing and the settled volume (SV) for the other part (Fig.5.).

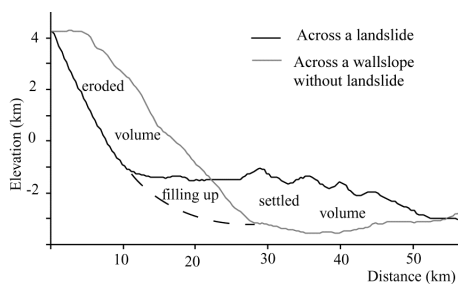


Fig.5. The two types of computed volumes

These two types of volume were estimated in 3D for each landslide by DEM subtraction between a DEM

covering the landslide zone and a pre-landslide DEM constructed for each landslide from the topography of the unslided wallslopes on the both sides of the landslide. A part of the settled volume has filled up a part of the eroded volume at the foot of the scarp. This volume, that we have called "filling up" is an important part of the total displaced volume and was added to both types of volume. With the two types of volume, volume balances were also computed.

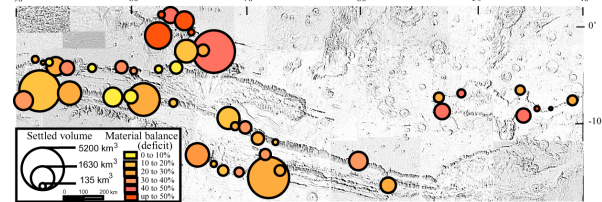


Fig.6. Distribution of the volumes and volume balances within Valles Marineris. The areas of the circles are proportional to the settled volumes. Colours gradation correspond to increasing classes of material deficit.

The settled volumes range from 50 km^3 up to 5000 km^3 . The eroded volumes range between 60 km^3 to 9000 km^3 . The volume balances display deficits ranging from 5 % for the more equilibrated balances and up to 70 % for the largest deficits. The landslides with the largest volume deficits are located in Hebes Chasma. All the five landslides of this canyon have a material deficit larger than 50%. Hebes Chasma is an enclosed canyon where material exportation after the landslide can not explain this deficit. These deficits could result from the porosity of the landslide source supporting the karstic origin hypothesis [8] of this kind of canyon.

Ages of Valles Marineris landslides: Valles Marineris landslides were dated by Lucchitta [2] from Viking images. At the spatial resolution of these pictures, only few landslides are affected by impact cratering. All the landslides of V.M. have been dated by a unique crater count. This crater count assumed that the landslides were contemporary. The results displayed an early event in the history of Valles Marineris.

MOC high spatial resolution images covering the landslide deposits are now available and show a large range of crater density. For most of V.M. landslides, several MOC images cover their deposit and allow us to estimate an age for each landslide. In order to have some chronological markers, crater counts were also made on MOC images covering the canyon's floor near landslides.

The example presented on Fig.7 is located within Gangis Chasma. The deposit is at least constituted by three landslide events with debris aprons. The main debris apron covers at the East a second underlying apron probably coming from a previous landslide.

Crater counts on both debris aprons and on the canyon floor were realized.

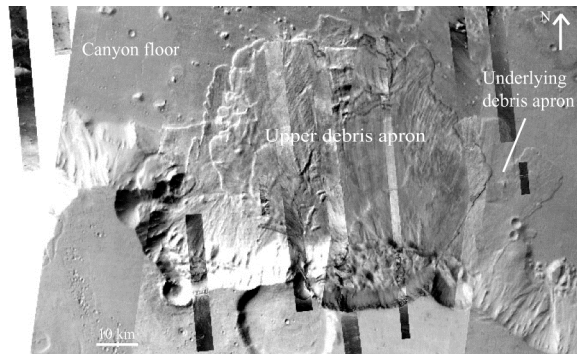


Fig.7. Localisation on a THEMIS images mosaic of the MOC images used to date the floor of Gangis Chasma, the underlying debris aprons and the upper debris aprons of a Gangis Chasma landslide.

The results of crater counts on images covering the floor follow the isochrones of absolute ages. The distribution of crater count correspond to an age between 2.5 Gy and 3 Gy (Fig.8). This age means that this region of Gangis Chasma did not submit to resurfacing process after the formation of the 2.5 Gy old floor surface. The distribution of crater count corresponding to the underlying debris apron also follows the isochrones implying an age between 1 Gy and 2 Gy (Fig.9). The crater count results for the upper debris apron follow the isochrones giving an age between 10 My and 100 My (Fig.10).

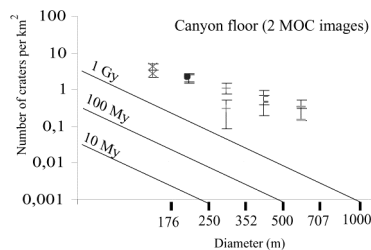


Fig. 8. Result of crater counts on 2 MOC images covering Gangis Chasma floor. Absolute ages are taken from Hartmann et al. [9].

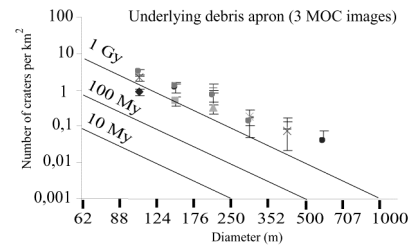


Fig. 9. Result of crater counts on 3 MOC images covering the underlying apron of a Gangis Chasma landslide. Absolute ages are taken from Hartmann et al. [9].

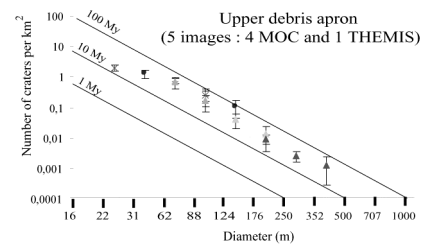


Fig. 10. Result of craters count on 5 MOC and THEMIS images covering the upper apron of a Gangis Chasma landslide. Absolute ages are taken from Hartmann et al. [9].

This chronology of events implies that landslides correspond to distinct events during time and that the activity period of these landslides spread out in the time up to the lower 100 My history of Valles Marineris. These results are in agreement with the dating of about 40 other landslides of Valles Marineris. The triggering mechanisms are then reproducible during the time. The seisms induced on Mars by impact cratering or by a continuous tectonic activity within Valles Marineris are reproducible mechanisms.

Conclusion : The morphological study reveals that landslide morphologies display fluidization features (thin debris aprons, mobilities...). The volume balances computing on the landslides are always deficient. It can be interpreted as large porosities in the landslide sources. Then, the question of the presence of fluids filling up a part of the regolite porosity of the landslide dynamic could be raise. The ages of the landslides spread out in the time up to recently. These results reinforce the hypothesis of seism triggering landslide (by impact cratering or tectonic activity). This large activity period during the time also implies that they are available fluids in the martian regolite to produce fluidization morphologies up to recently.

References: [1] Lucchitta B.K. (1978) *Geological Society of American Bulletin*, 89, 1601-1609. [2]

- Lucchitta B.K. (1979) *JGR*, 84, 8097-8113. [3]
McEven A.S. (1989) *Geology*, 17, 1111-1114. [4]
Baratoux D. et al. (2002) *GRL*, 29 (7), 60-1 60-4. [5]
Shreve R.L. (1966) *Science*, 154, 1639-1643. [6]
Legros F. (2002) *Engineering Geology*, 63, 301-331. [7]
Harrison K.H. (2002) *LPS XXXIII*, Abstract #1432. [8]
Carr M.H. (1996) *Water on Mars*, Oxford Univ. Press.
[9] Hartmann W.K. (2003) EGS-AGU-EUG, Abstract
V.5 n°07354.

THE EFFECT OF CONVECTIVE ADJUSTMENT ON THE GLOBAL CIRCULATION OF MARS AS SIMULATED BY A GENERAL CIRCULATION MODEL. S. C. R. Rafkin, *Dept. of Space Studies, Southwest Research Institute, Boulder CO 80302, USA, (rafkin@boulder.swri.edu).*

Many Mars Global Circulation Models (MGCMs) use convective adjustment to simulate the process of subgrid-scale mixing in the convective boundary layer. Three important underlying assumptions for convective adjustment are: 1) that the atmosphere instantaneously removes potential energy contained within an unstable stratified atmosphere; 2) that there exists an equilibrium between the generation and consumption of potential energy; and 3) that the kinetic energy generated due to circulations that remove potential energy may be neglected. These three assumptions are generally reasonable for global circulation modeling of the terrestrial atmosphere, from which the Mars modelling community has its roots. However, there is observational, theoretical, and numerical modeling evidence that one or more of the assumptions underlying the convective adjustment process are grievously violated in Mars' atmosphere.

Vertical redistribution of atmospheric entropy via convective adjustment will result in a redistribution of the vertical pressure gradient. Thus, convective adjustment in adjacent

atmospheric columns will generally result in an altered horizontal pressure gradient. It is the horizontal pressure gradients that drive the wind. Consequently, it is easy to envision how convective adjustment might alter the simulated atmospheric circulation with MGCMs.

Although the underlying assumptions for convective adjustment may not be satisfied for MGCMs, it is unclear whether the convective adjustment process results in spurious or inaccurate climate statistics. Convective adjustment has the beneficial property of helping to keep MGCMs numerically stable and consistent with the governing hydrostatic dynamical equations. Therefore, if convective adjustment has little or no effect on the MGCM results, than it might be retained strictly for numerical purposes.

A set of experiments with convective adjustment on and off would provide insight into the effects of convective adjustment within MGCMs. Results from such experiments conducted with the NASA Ames MGCM are presented.

MODIFIED IMPACT CRATERS - CLUES TO MARTIAN GEOLOGICAL PROCESSES. J. Raitala¹, M. Aittola¹, V.-P. Kostama¹, H. Lahtela¹ and T. Öhman², ¹Planetology Group, Astronomy, Dept. of Physical Sciences, FIN-90014, Univ. of Oulu, Finland, ²Institute of Geosciences, Dept. of Geology, FIN-90014, Univ. of Oulu, Finland. (jouko.raitala@oulu.fi)

Introduction: The most basic type for a small impact crater is a circular bowl depression surrounded by an elevated rim and an ejecta blanket with inverse layering, secondary impact craters and long-reaching thin ray deposits. In the case of larger impact craters and basins this picture is more complicated by a central uplift and internal rings, respectively. The main appearance of the impact craters on the Martian surface depends on the size, mass, velocity, type, and impact angle of the projectile and on the amount of the impact energy delivered into the surface bedrock [1].

In nature, however, there are hardly any two totally identical impact craters or basins. Any deviation from the circular or regular crater shape has a reason and, in many cases, this reason relates either to the bedrock geology or to active geological processes. This fact can be utilized in identifying some of the characteristics and development phases of the Martian geological environment, which has not only interacted in the impact event but also influenced in the subsequent impact crater modification. Every deviation from the regular crater form is based on a reason, which may also be a geological one. The best known examples are the rampart craters with their characteristic ejecta blanket and high or wide central peak which all tell us something of the Martian wet or permafrost-rich environment in the past [2]. This and other impact crater modifications can be found to provide crucial information of the local surface geology, bedrock properties and, more generally, of the geological evolution phases of the area studied [3,4].

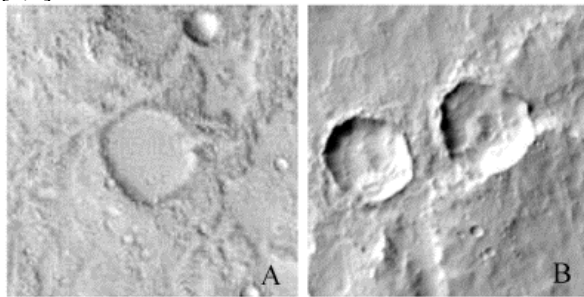


Figure 1. Polygonal craters near Isidis Basin, **A.** with four straight sides THEMIS I00983005, 1,5 km x 1,5 km; **B.** with hexagonal shape THEMIS I01747003, 30 km x 30 km.

Straight crater walls: The bedrock properties have resulted in additional effects during the immediate impact event by producing small polygonal impact craters (Fig. 1). The linear rim segments are partly controlled by the bedrock fractures, lineaments or zones of weaknesses because the excavation of the crater progresses more easily along a plane of weakness than in other directions [i.e. 1,5]. On Mars, there are numerous Bar-

ringer-type simple craters with linear crater rim segments which, in spite of the huge amount of energy released in the impact, indicate bedrock tectonics, especially if studied systematically [6].

In the case of the larger complex craters the share of the post-impact rim modifications is far more common and also controlled in a more straightforward way by the tectonic bedrock properties. The massive rim slumpings have a clear tectonic control, which can also be studied statistically to infer the fractures in the target bedrocks. Collapses of the rim take place along planes of weakness in the target [1]. The dominant areal fracture directions can thus be directly measured from the orientations of the straight rim segments in complex polygonal craters (Fig. 2; [6]).

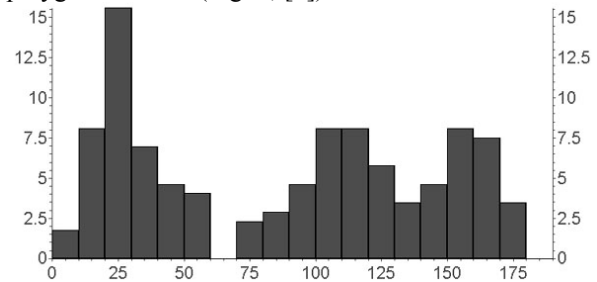


Figure 2. Percentages of rim strike directions of polygonal craters SW from Isidis (2°N-14°S, 272°W-288°W), n=173.

Crater erosion and age: In principle, it is well established how relative ages of a series of certain impact crater with similar diameters can be defined and utilized in estimating geological events and properties within limited study areas. At first, all Martian erosion processes decrease the observability of individual crater details thus slowly destroying the crater itself towards and beyond the recognition limit (Fig. 3, from A to D). Within a single geological unit the disappearance rate can be estimated to be the same for similar-size craters and can therefore be used to determine qualitatively the effects of various geological processes involved as well as the relative ages of the appropriate impact craters and their immediate environments.

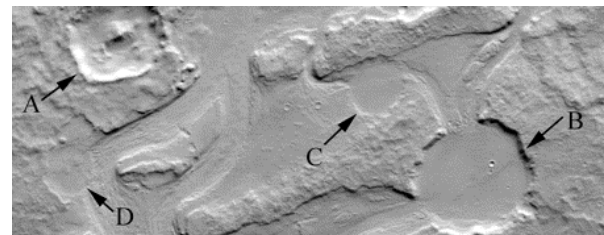


Figure 3. Labou Vallis enters to several impact craters and forms a lake chain. The craters have prominently smooth interiors and distinct inlet/outlet channels. Notice the gradual disappearance of crater details (A-D). Fragment of THEMIS I02277010, 32 km x 80 km.

It can also be observed how the increasing surface age increases the number of visible impact craters and thus also the amount of impact erosion within the Martian highlands. This may lead up to the situation where the saturation number of craters is reached with a certain diameter and the continuing impact flux moves this saturation diameter into the direction of larger craters along the time. Due to the effective erosional-sedimentational processes on Mars, only part of this saturation can be observed on the highland units where it can be further used to estimate the lower limits of the effects of various-type erosion rates.

On the other hand, it is very easy to define the areas with a lack of large impact craters or where they are totally missing. The diameters of the largest or smallest impact craters still possible to be identified as such provide us with some important details of the effectivity - and sometimes also of the type - of the resurfacing processes present [7].

It is thus critically important to understand the effects of any really important geological agent in each of the different Martian environmental sub-units because this environment-depended factor may have strongly effected the history of impact craters in a particular location [4]. Some of the processes may still effect to the present crater modification [cf. 8,9].

Fluvially modified craters: Many of the studied craters found from within the greater Hellas Basin area, for example, have undergone substantial fluvial processes (Fig. 3). If the surviving geological features of the studied impact craters are preserved well enough, the share of this fluvial erosion-sedimentation cycle in modifying the craters can be recognized and utilized in studying the water-related history of Mars. In many cases we can take an optimistic view of our ability to identify traces of fluvial processes because many such Martian impact craters are preserved rather well due to their relative youth and/or partly due to the relative dryness of the more present Mars.

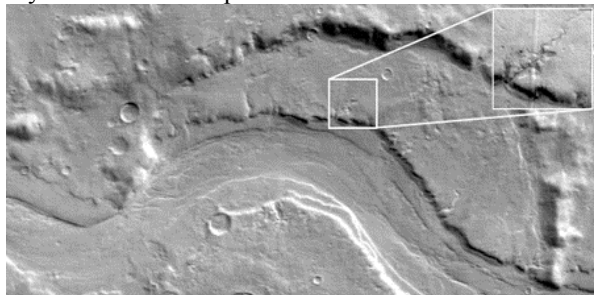


Figure 4. Image shows Reull Vallis cutting through an eroded crater. Image is a fragment of THEMIS I01657002, 31 km x 60 km. The detail of a sapping side channel is part of V01657003, 6 km x 6 km.

In some cases, the major outflow channels have cut across the craters and surface units without any significant indication of effects to the crater structures. It can be seen how a deep erosion channel curves across the eroded low-rim crater with an otherwise smooth interior (Fig. 4). An interesting detail is seen on the crater

floor beside the main channel where the numerous small sapping-type channels indicate the existence of layered interior material and previous ground-liquid flows along some interlayer surfaces.

The abundance of layered units on the crater floors can be seen in some MOC and THEMIS-VIS images. The etched terraces and deposits reveal parallel horizontal layers (Fig. 3). This kind of layering may have been caused by several sedimentation processes but in the cases where there are adjoining large-to-medium size flow channels flowing into the crater, a realistic reason for the observed layering could be the existence of flow-related sedimentation. This is particularly obvious in the cases where there have been several sediment-feeding channels, smooth crater interior, and an additional outflow channel representing the site and time when the ponded flow material finally broke its way through the lowest or weakest part of the rim after a short or a lengthy period of reservoir time (Fig. 3). These cases show, that the effectivity and period of time of Martian fluvial activity have been large and long enough, respectively, for substantial amount of sedimentation at least in certain areas.



Figure 5. Delta-like structure at the end of a channel entering impact crater through a wide U shape opening in the crater rim east of Mangala Valles. Fragment of THEMIS V02540002, 5 km x 8 km.

Slightly closer to the present or within the locations with less water activity, there are impact craters with smaller eroded rim channels as seen from numerous craters locating on the western highlands of the greater Hellas area. Their interior slopes have numerous fluvial channels varying in length from 10 to a few tens of kilometers only. The one-to-a-few kilometer wide channels originate either from the upper rim area or from the surrounding highlands. The floors of such craters display a relative smoothness. This, together with the fact that the flows have eroded an amount of rim material and moved it downslope, most probably indicates the existence of sedimentated flow-related floor material representing the period of time of larger fluvial activity. In certain places there are later delta- or apron-type masses in the channel ends on the top of the smoother interior sediments indicating the effects of the

later flow units with lesser amount of liquid material (Fig. 5).

Many craters are modified by still more recent fluvial processes. Snow or a liquid material have been proposed to have been important in deforming layered crater rims in certain poleward-looking locations [cf. 8,9]. Such flow features typically begin from within alcove depressions with seasonal snow or source wells, resulting in lengthy channel-like down-slope erosion, and ending in apron-like cumulation pilings.

Crater sedimentation: In addition to the erosion effects of the channels flowing through the crater, they may also deposit material into the craters. This is especially true when many of the craters described above have been temporary water reservoirs during the period of time when the inflow has partially filled them and before the water level rise has given way to the outflow channel formation. Depending on the amount of water and erosion and also on the repeated occurrence of the inflow involved, this lacustrine phase has resulted in layered sediments on the crater floor. This process smoothens the crater interiors and may create deep water-saturated layered materials for the subsequent permafrost formation. The existing permafrost may further add debris apron type mass movements inside the crater rims.

Together with the decreasing inflow into the crater its sedimentation effect also diminishes. The final phase which still carries some amount of solid material to deposit just in front of the inflow channel is seen as a delta formation (Fig. 5; see also [10]). In some cases a wider and thinner delta layering may be visible, possibly due to a stronger final inflow pulse. In places we can identify a smaller and more local triangle-like delta piling which may have formed into the mouth of a smaller and/or steep-sloping inflow channel.

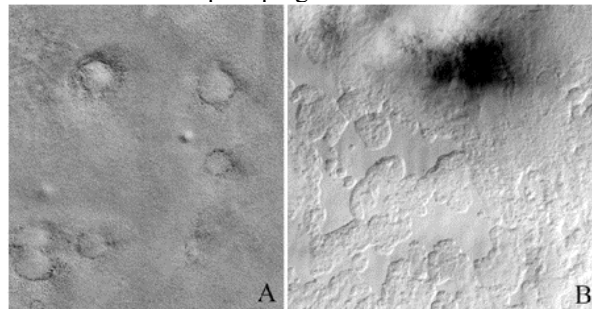


Figure 6. **A.** Example of mantled craters within high latitudes. Notice the gradual change and disappearance of crater topography. Fragment of MOC E0500602, 3 km x 3 km. **B.** Dissected mantle material on the bottom of a crater next to the central peak. Crater is located in the highlands south of Hellas Basin. Fragment of THEMIS V01209003, 10 km x 10 km.

The eolian activity may also have filled the craters. The deposits of wind-blown materials may consist of rather even layers (Fig. 6a) of dust particles or dust-ice aggregates which, due to their small size and low density, are easily transported by Martian winds and storms. Many craters may have served as a previous

deposition traps for this material as seen from the now-exposed horizontal sedimentary layers (Fig. 6b) even in craters which do not have any recognizable inflow channel at all.

The importance of an eolian process in changing the crater is still more visual in the cases where we are able to identify dune fields within the crater floors. These dune fields may differ in size and importance. They may also differ in ages beginning from the more ancient paleodunes to the present still-moving dunes (Fig. 7a). Being the most surficial units, the dune fields may cover previous formations, structures and layers but also they may, in places, have been effected by other geological crater-modifying processes.

Volcano-tectonic effects on impact craters: For some of the impact craters the proximity of a volcano emphasizes the importance of the crater location in identifying its post-impact modification. It is known from numerous planetary, also Martian, craters that the formation of a large crater has generated new or re-opened old fractures in the bedrock and thus opened trespassing channels for magmas to erupt onto or intrude into the planet's crust.



Figure 7. **A.** Pit depressions and paleodunes on the floor of Rabe Crater. Part of THEMIS I02471002, 30 km x 30 km. **B.** Possible pyroclastic layering within a crater north of Hadriaca Patera. Fragment of MOC M0303051, 0.8 km x 0.8 km.

There are also plenty of impact craters which have been partially buried by pyroclastic deposits (Fig. 7b). The low Martian gravity and atmosphere pressure have favoured the explosion-type volcanic eruptions which have been very effective to spread various types of volcanic pumices, scoriae and tephra over wide areas around these patera-type volcanoes. The approximate depth range of the pyroclastic deposits in various distances from appropriate volcanoes can be estimated from the amount of the impact craters fill related to the actual numbers for depth-diameter ratios of impact craters inferred for different crater sizes in the Martian environment.

In the close vicinity of a volcano the pyroclastic layer depth may exceed the height of the highest crater rim, a situation which allows only the minimum deposit depth estimation using the depth-diameter ratios of impact craters. This may also be very true when estimating the lava depths within volcanic planitiae. Lavas which have renewed the whole surface by cover-

ing all the impact craters beyond identification may be much thicker than required to cover just the crater rim peaks (cf. Tharsis). Some other Martian environments, however, display graphically impact crater rim rings partially covered by lava flows. This allows us to estimate the depth of these lavas and thus the total amount of extrusives or, if the period of time is inferred, the extrusion rate.

There are, however, some certain areas on Mars where even totally lava-covered impact craters can be utilized in studying the local geology. Hesperia Planum has a very complex network of tectonic structures consisting of compressional wrinkle ridges. These linear structures were generated along previous zones of weaknesses or sub-lava hill crests during the surface shortening of the large lava-covered area [11]. There are also a high number of circular wrinkle ridges which must have a connection to the lava-covered topography, too. An explanation for their formation involves the existence of a previous impact craters. The extruding lavas have covered these craters totally but the lava thickness is deeper over crater floors and other depressions and thinner over the crater rims. During the sinking or areal shortening tectonic phase the compressional forces break the lava cover most easily in places where it is thinnest, i.e. over the buried impact crater rims. The existence of lava-preceding loose surface material or breccia layer increases the incompatibility between this and the later lava coverage. A more straightforward connection between tectonic bedrock directions and wrinkle ridges locating within the floors of some impact craters has also been found [12].

Glacial features in impact craters: There are numerous U-shape openings through the impact crater rims. Some of them do not have any indication of a fluvial channel and another ones have such a very minor channel only which is unable to explain the erosion required to make the U-valley (Fig. 5). The U-shape valleys have a distinct topography and, on terrestrial glacial environments, they are known to have formed by glacial movements.

There are also strange pit depressions [13], which decorate some of the impact crater interiors, especially on the highlands to the west of Hellas Basin (Fig. 7a). The geological processes involved in formation of these identified angular depressions in the crater interiors are still unknown but might involve events related to sublimation and melting of the sediment- or dust-buried ice blocks or permafrost layers. There may also have been some other still-unknown geological processes involved.

Even if we do not see any clear evidences of the present glaciation processes on the Martian surface except the two polar caps and possibly the adjoining mantle-terrain areas the above-mentioned observables may increase our understanding of the ancient ice-rich phases of Mars. These crater-modifying topographies

have to be studied together with the facts that there has been plenty of water in Mars, large-scale climate and temperature variations, and large variations in the direction of the rotational axis of Mars. Each of these facts, together with the observed existence of definitive steep-slope mesas or tuyas [14], possible glacial-related formations on the mountain slopes [15], and the crater-related U-valleys and pit depressions described, contribute to the evidences of the possible existence of previous Martian glaciations, which may have taken place varying in their location or time or both. We have, however, to look for further additional evidences of various types of glacial crater modifications before we can conclude for sure that this has also been the case on Mars.

Conclusion: Many of Martian impact craters may provide us with evidence of the bedrocks or active geological processes involved in the cratered surface units. We only have to read the story right by interpreting the peculiar impact crater details correctly, by putting the topographic surface formations of modified impact craters into their right environmental context, or by investigating the diversity of studied crater phenomena using various statistical approaches.

It is difficult to draw geologically sound conclusions based only on a small number of impact craters and their structures. We usually need to study a wider area with several or numerous impact craters in order to gain a deeper insight of what geological events may have been involved in the evolution of this particular area. Studies of modified impact craters and their details then become more important either in providing the additional supporting details required in confirming the evolving ideas of the areal geological phases and their importance or, on the other hand, in giving a first hint or suggestive peculiar surface expression of a geological process the presence of which has been previously mostly neglected or misunderstood within a particular Martian area.

The study calls for new creative approaches in utilizing the Martian impact crater realm in order to understand and investigate its geological phases, epochs and processes in a more detailed and complete way, and to improve the ideas of Martian global and areal geological development.

References: [1] Melosh, H.J. (1989) Impact cratering: A geological process. Oxford Univ. Press, NY. [2] Carr M.H. et al. (1977) JGR 82, 4055-4065. [3] Aittola, M. et al. (2002) LPS XXXIII, Abstract #1485. [4] Öhman, T. et al. (2002) LPS XXXIII, Abstract #1270. [5] Baldwin R.B. (1963) University of Chicago Press, Chicago London, 488 pp. [6] Öhman, T. et al. (2003) LPSCXXXIV, Abstract #1311. [7] Kostama, V.-P. et al. (2003). LPS XXXIV, Abstract #1340. [8] Malin, M. C. and Edgett, K.E. (2000). Science 288: 2330-2335. [9] Costard, F. et al. (2002) Science 259: 110-113. [10] Cabrol, N. A. and Grin, E. A. (1999). Icarus 142: 160. [11] Raitala, J. (1988). EMP 40: 71-99. [12] Raitala, J. and Kauhanen, K. (1992) EMP, 58: 65-78, 1992. [13] Schultz, P. and Glicken, H. (1979) JGR 84, 8033-8047. [14] Ghatan, G. J. and Head, J. W. (2002) JGR 107, E7: 2. [15] Head, J. W. and Marchant, D.R. (2002). Vernadsky-Brown Microsymposium 36, Abstract #029.

EVIDENCE FOR MARS REGOLITH PRESERVED IN SHERGOTTITE EET79001: DIFFERENTIAL COMMUNITION AND CHEMICAL WEATHERING RECORDS. M.N.Rao¹ and D.S.McKay², ¹Lockheed Martin, 2400 NASA Road One, Houston. TX.77058, ²NASA Johnson Spae Center, Houston. TX. 77058. (e-mail: david.s.mckay@Jsc.nasa.gov).

Introduction: Earlier, we pointed out that some shergottite impact melt glasses contain large abundances of Martian atmospheric noble gases and show large variations in ⁸⁷Sr/⁸⁶Sr (initial) isotopic ratios. These samples likely contain Martian regolith fines (MRF) [1-3]. We showed that one of the characteristics of these MSF fractions is the simultaneous enrichment of felsic component and an associated depletion of the mafic component relative to the host phase in which these glasses are located. In several samples studied by us, the magnitude of enrichment and depletion is found to vary from one sample to the other. In addition, these samples show evidence for the occurrence of secondary sulfate mineral phases due to aqueous alteration near Mars surface. As the basaltic shergottites presumably originate from near-surface regions of young volcanic terrains such as Tharisis (Olympus Mons) or Elysium Mons [4], the MSF fraction embedded in these impact glasses likely provide clues regarding the physical and chemical weathering environment to which their precursor soils were exposed near the Martian uplands prior to the impact-melt generation.

We suggested earlier that the felsic enrichment and mafic depletion observed in these samples is related to the occurrence of the Martian regolith fine fraction in them [3]. These glasses contain varying amounts of the MRF fraction and the relative ratios of the coarse and fine fractions in these impact glasses determine the magnitude of the enrichment and depletion factors in these samples. On comparison of our results with those obtained in the laboratory simulation bombardment experiments on gabbro using projectiles with similar impact velocities on Moon/Mars by Horz et al. [5], we found that, though the patterns of enrichment and depletion of the element-oxides in the samples are similar, but their magnitudes are grossly different. In the Horz et al. experiments, the finer size fractions were enriched in AL₂O₃ relative to the starting composition and were depleted in FeO and MgO. If we assume that melt glass pocket ,507 originally consisted entirely of fine-grained regolith developed on the host rock represented by EET79001 (lithology B), can we explain the difference in chemistry entirely by differential comminution and mechanical concentration of the fines? When we compare the melt glass composition in EET79001 to the bulk rock composition, we find the same trends shown by Horz et al. [5], but they

are much more enhanced. If the regolith material which was the precursor to the melt glass originally consisted of fine-grained regolith, differential comminution concentration of the fines by mechanical fractionation could explain the trends, but not the magnitude of the chemical difference. Consequently we conclude that, while differential comminution and mechanical fractionation may have operated, there must be other processes operating on Mars responsible the significant difference in composition between the melt glass and the bulk rock. In this study, we examine this aspect in detail and show that these differences could be explained by chemical (acid-sulfate) weathering of the soil fines near the martian surface by aqueous solutions containing acidic volatiles such as SO₂ and H₂O released in volcanic eruptions during the last few hundred million years on Mars [6,7].

Experimental: Several impact melt glasses in shergottites were studied by us using a Cameca SX100 state-of-the-art microbeam automated Electron Microprobe at JSC using standard analytical and calibration procedures described earlier [1-3]. We discuss below data obtained on an impact-melt glass inclusion ,507 from EET79001 and compare the results with those obtained on Shergotty glasses (sample provided by Don Bogard).

Results and Discussion: We studied earlier several veins and pods in impact-melt glass samples ,77 ,78 ,18 and ,20A in EET79001 and averaged all the data points in these veins. The average values are plotted in Fig.1 of [2] where we found significant enrichment of Al₂O₃ and CaO relative to the bulk rock containing these melt pockets (Lith A) and much larger depletion of FeO and MgO relative to Lith A. SO₃ abundance varied from 0.4 to 1.6 showing modest enrichment relative to Lith A. These values represent averages of about 900 data points obtained in the line profiles across the veins. In the present study, we focuss our attention on the Electron Microprobe and SEM data gathered along several line profiles in the veins and pods of impact melt glasses of ,507 of EET79001 (Lith B).

The FeO & MgO as well as Al₂O₃ & CaO abundances are plotted against SO₃ in Figs. 1 & 2 respectively. In Fig. 3, SiO₂ is plotted against SO₃. At some analysis sites, we found SO₃ contents as high as ~16%, a value more than twice as high as the SO₃

content of Viking and Pathfinder [8,9]. The SO_3 vs FeO plot in Fig.1 where SO_3 varies from about 0.6% to 16%, shows excellent positive correlation between the two elements. When we extrapolate the correlation line back to $\text{SO}_3 = 0.5\%$, the FeO content of the mineral assemblage in the glass turns out to be $\sim 10\%$. This indicates that the FeO content of the precursor soil fines in the impact glass is depleted by $\sim 50\%$ relative to the host bulk rock. Further, in the Al_2O_3 vs SO_3 plot in Fig. 2, the data points show negative correlation between these elements. When we extrapolate the correlation line, as before, to $\text{SO}_3 = 0.5\%$, we find the Al_2O_3 content in the starting materials to be $\sim 20\%$. This indicates that Al_2O_3 is enriched by a factor of 2 relative to the host phase. If we consider that these enrichment and depletion factors are only due to comminution of basaltic rocks due to meteoroid bombardment, then the observed values found here are very high compared to those obtained by Hoerz et al. [5] in the simulation experiments on gabbro. These results suggest that there may be an additional process operating on these soil fines on Mars. The most likely candidate for such a process is chemical weathering of soil fines near Mars surface. We explore below the conditions and the consequences of acid-sulfate weathering of soil fines near Mars surface during the last few hundred Ma.

Acidic Volatiles: Based on the resurfacing rates on Mars, Tanaka et al.[10] estimated that the volcanic eruptions on Mars took place once in every 10^4 years during the last few hundred Ma. During these volcanic eruptions/emnations, huge amounts of volcanic gases consisting of water and sulfurous gases (among others) are released into the atmosphere where SO_2 is oxidized, converted to H_2SO_4 and deposited as aerosols on rock surfaces [6,7]. Because of the large surface area of the comminuted fine basaltic materials near the volcanic eruptions, these acidic volatiles chemically react with the constituent mineral components resulting in slow dissolution and chemical (acid-sulfate) weathering. Here, we examine the nature and conditions of dissolution and reprecipitation of secondary mineral phases during acid-sulfate weathering of ferromagnesian minerals and feldspars in the Martian regolith.

Chemical Weathering : To study the nature of chemical weathering effects on ferromagnesian minerals by acid-sulfate solutions, we use the FeO and MgO vs SO_3 plot in Fig. 1. The Fe-Mg silicates rank highest in order of vulnerability of igneous minerals to chemical weathering reactions, with feldspars being

next in order [11]. When the pyroxenes are degraded by acid-sulfate solutions, the Fe^{+2} and Mg^{+2} go into solution along with silicic acid. It may be noted that the oxidation of Fe^{+2} to Fe^{+3} is extremely slow on Mars compared to Earth because of very cold temperatures near Mars surface. The excellent positive correlation between FeO and SO_3 indicates that iron may be precipitated as ferric hydroxy sulfate which is relatively insoluble. Note that the potassium abundance in our samples is very low which does not favour the precipitation of K-jarosite /alunite in these samples [6, 7]. Also, note that sulfur predominantly exists as sulfate in these samples [2,12,13].

At low SO_3 values, both FeO and MgO in this melted regolith (507) are highly depleted relative to the host rock (Lith B). This observation suggests that The chemical weathering appears to have been a three step process. First (step 1) MgSO_4 and FeSO_4 were formed as a result of acid-sulfate degradation of pyroxenes.. Second (step 2), the regolith was partially leached of these components; they were possibly removed from the system by transgressing aqueous solutions seeping into the top portions of Martian regolith, a process which decreased their concentration and increased the concentration of Al_2O_3 in the residual soil. During step 2, some SiO_2 is removed in solution. We hypothesize that as acid-sulfate solutions degrade pyroxenes and feldspars, some SiO_2 goes into solution as H_2SiO_4 and it is removed from the system by the transgressing solutions. Finally (step 3), a solution was reintroduced into the soil and precipitated the SO_3 phase along with a considerable amount of FeO and a slight amount of MgO, presumably as sulfates. During step 3, some components such as Al_2O_3 may also have been removed to a slight degree. The behaviour of feldspars in the soil precursors under these acidic conditions on Mars can be deciphered from the correlation lines in Al_2O_3 and CaO vs SO_3 plot in Fig. 2. Both Al_2O_3 and CaO negatively correlate with SO_3 suggesting that the dilution effect is significant in bothcases. The decrease of CaO with added SO_3 can almost entirely be explained by the dilution effect (closure), but only about half of the decrease of Al_2O_3 can be explained by dilution. Consequently, the data reflect a real decrease (removal) of Al_2O_3 by weathering and transport during step 3. Further, in Fig. 3, we show good correspondence between SO_3 and SiO_2 . We find that as the SO_3 content increases from 0.5% to $\sim 16\%$, SiO_2 decreases from $\sim 50\%$ to $\sim 40\%$. Most of this variation of SiO_2 can be explained by dilution.

Note that MgO remains relatively flat over the complete range of SO_3 . Dilution alone would cause

MgO to decrease about 16% as SO₃ increases, but this decrease is not observed. Therefore, MgO is actually increasing slightly in step 3 with the introduction the SO₃-rich material along with FeO. However, it had been partially dissolved and leached out in step 1 and 2.

Model calculations : We present a model based on the above results and carry out calculations ,under the assumptions discussed below. We start with shergottite basaltic composition of 56% pyroxene and 29% feldspar plus maskelynite for EET79001 [14]. This material is comminuted by meteoroid bombardment on Mars producing fine-grained regolith fractions where felsic component is slightly enriched and mafic component is depleted relative to the starting material. In our model, we use the enrichment and depletion factors given by Horz et al. [5]. We assume that all FeO and MgO in the solution results from the dissolution of pyroxenes and all Al₂O₃ in the solution comes from the dissolution of feldspars. CaO is contributed equally by the dissolution of pyroxenes and feldspars into solution. In this model, the acid-sulfate solutions are generated from acidic-volatiles released in volcanic eruptions into the atmosphere[6, 11]. They interact with the enriched/depleted starting basaltic fine material by dissolving varying proportions of pyroxenes and feldspars depending on the acid-sulfate availability under restricted aqueous conditions. We consider three cases in our calculation : Case A = 8% pyroxene and 4% feldspar dissolved into the transgressing solutions where the resulting MgSO₄, H₂SiO₄, and Al₂(SO₄)₃ are removed from the system and an equivalent amount of iron sulfate is reintroduced and precipitated as insoluble Fe₂(SO₄)₃ on the residual grains. Case B = 16% pyroxene and 8% feldspars dissolved (and the rest of the details are same as above). Case C = 32% pyroxene and 16% feldspar dissolved (and the rest of the details same as above). We assume that when iron dissolves it goes into solution as FeSO₄ and when it precipitates, it leaves the solution as Fe₂(SO₄)₃. Using these model steps in dissolution and precipitation reactions, we calculate the composition of different element-oxides in the end products. We plot these calculated values (model-dependant) in Figs. 1, 2 and 3. The agreement between the experimental and calculated values is good. All trends generated by the model correspond to trends of the actual measured data. This observation indicates that these glasses contain locally-produced fine-grained Martian regolith which had undergone acid-sulfate weathering and fractionation under limited aqueous conditions.

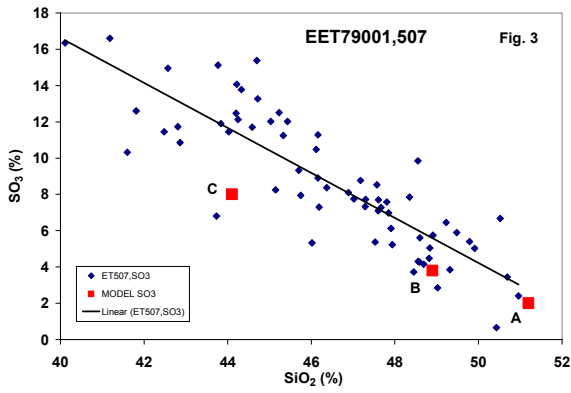
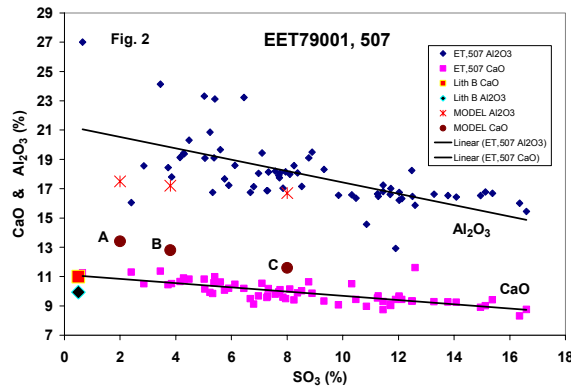
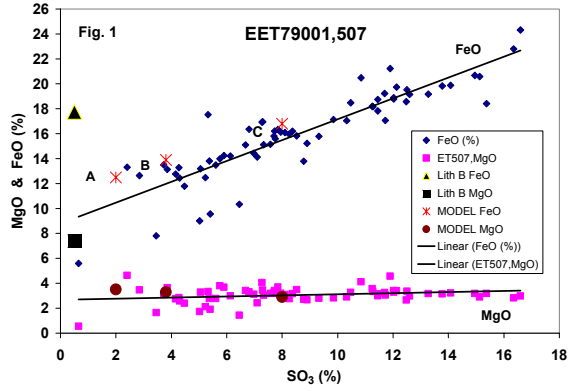
Conclusions: We find that the composition of the gas-rich melt inclusion (,507) shows systematic varia-

tions from the host rock (EET79001, Lith B) that can be explained by a multi-step history consisting of differential comminution with some chemical fractionation, acid/sulfate dissolution, removal of some components, and introduction of sulfates, mainly Fe but also minor Mg. This regolith was then melted and mixed with Lith B, trapping the gas-rich melt in pockets, presumably during the impact that ejected the sample from Mars. Similar chemical trends (not shown here) found in a gas-rich glass inclusion in Shergotty suggest that this weathering sequence may be repeated at other martian locations.

References: [1] Rao M.N. et al. (1999) *GRL*, 26, 3265-3268. [2] Rao M.N. and McKay D. S.(2002) "Unmixing the SNCs", *LPI Contribution No.1134*, pp.49-51. [3] Rao M.N. and McKay D. S.(2003) *LPS XXXIV*, #1252. [4] Nyquist L.E. et al. (2001) 'Chronology and Evolution of Mars', 96, 105-164. [5]. Horz et al. (1984) *Proc. LPSC. 15th, JGR, 89*, C183-C186. [6] Banin A. et al. (1997) *JGR, 102*, 13341-13356. [7]. Morris R.V. et al. (2000) *JGR, 105*, 1757-1817. [8]. Clark B.C. et al. (1982) *JGR, 87*, 10059-10067. [9] Rieder R. et al. (1997) *Science, 278*, 1771-1774. [10] Tanaka K.L. et al. (1992) *Mars* (eds. Kieffer, Jakosky, Snyder & Mathews) pp.345-352. [11] Burns R.G. (1993) *GCA, 57*, 4555-4574. [12] Gooding J.L. and Muenow D.W. (1986) *GCA, 50*, 1049-1060. [13] Clark B.C. and Van Hart D.C. (1981) *Icarus, 45*, 370-378. [14] McSween H.Y. Jr. and Jarosewich E. *GCA, 47*, 1501-1513. [15] McSween H.Y. Jr. and Keil K. (2000) *GCA, 64*, 2155-2166.

Figure caption: The FeO & MgO vs SO₃ plot (Fig.1) ; Al₂O₃ & CaO vs SO₃ plot (Fig.2); SiO₂ vs SO₃ plot (Fig.3) for EET79001,507 (Lith B). The positive and negative correlations are striking. For the details about the model compositions used in Case A, Case B and Case C which had undergone acid-sulfate weathering under restricted aqueous conditions, see text. The solid lines are least square trend line fits to the data.

.....



.....

ELECTRICAL DISCHARGES IN THE MARTIAN DUST DEVILS AND DUST STORMS. N. O. Renno, A. S. Wong, and S. K. Atreya, Department of Atmospheric, Oceanic and Space Sciences, University of Michigan, Ann Arbor, MI 48109-2143 (nrenno@umich.edu).

Introduction: The Mars Global Surveyor Mars Orbiter Camera (MOC) shows that aeolian processes have been actively modifying the surface of Mars [1]. The evidence of these processes in the form of wind erosion features, dust devils, and dust storms is abundant and visible even in images of the MOC wide-angle camera. Dust devils are ubiquitous features of terrestrial deserts and the martian landscape during the warm season. On Mars, dust devils are much larger and stronger than on Earth. Terrestrial dust devils have typical diameters of less than 10 m and are seldom higher than a few 100 m [2]. In contrast, dust devils with diameters between 100 m and 1 km, and heights of up to 7 km are frequently observed on Mars [1, 3]. Martian dust devils also have greater dust content than the terrestrial vortices. The dust devils observed in the images of the Mars Pathfinder panoramic camera have about 700 times the dust content of the local background atmosphere [4].

Regional dust storms occur rather frequently on Mars (Figure 1). In general, they are highly convective and many are similar to terrestrial hurricanes [5]. Sometimes regional dust storms grow and become global in extent. Enhanced dust devil activity might be a precursor of regional and global dust storms. There is evidence that regional and global dust storms frequently form in regions where theory predicts high occurrence of dust devils [6]. The theoretical framework applicable to convective vortices such as dust devils, waterspouts and hurricanes predicts that dust devils and dust storms have a higher probability of occurrence and are potentially more intense in regions of sloping terrain and large horizontal temperature gradients [6, 7, 8, 9], such as the region near the edge of the south polar cap during the warm season [8, 10, 11]. This is the region where regional and global dust storms are frequently observed [10, 12].

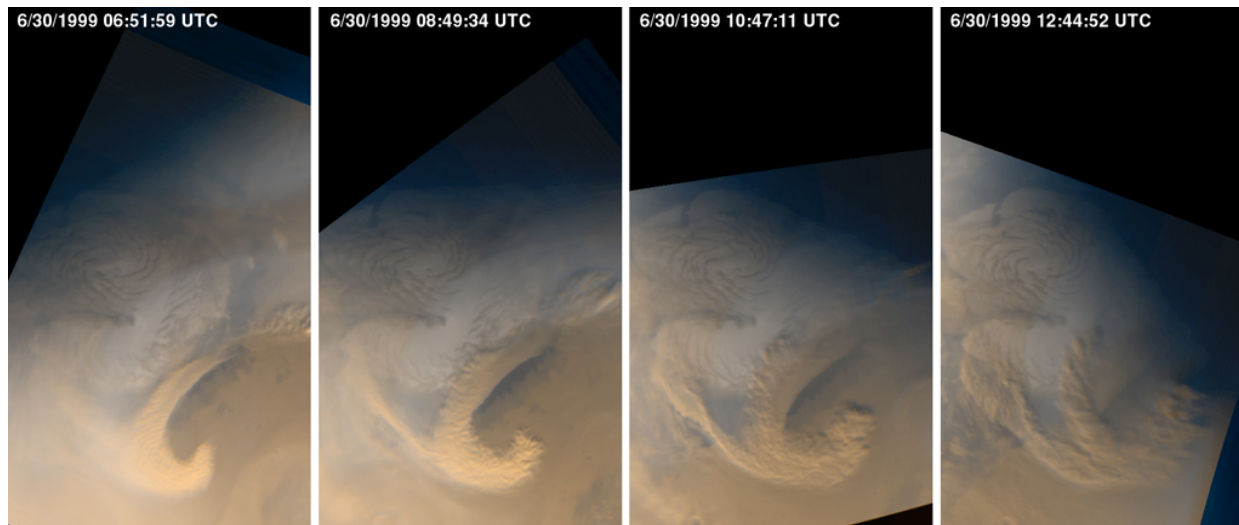


Figure 1. Mars Orbital Camera images of a regional martian dust storm developing at the edge of the north polar cap during the spring. This figure is a courtesy of NASA/JPL/Malin Space Science Systems.

Electrification of Dust Devils and Dust Storms: Triboelectric charging of saltating and colliding dust particles produces strong electric fields in terrestrial dust devils [13]. Electric fields in excess of 50 kV/m have been measured [14, 15]. All observations of terrestrial dust devils show negative charges aloft, and this distribution of charges agrees with the idea that negative charges are transferred to the smaller particles

during collisions [16]. Acceleration of charged particles and electrical discharges between them generate wideband electromagnetic radiation that can be detected by nearby radio receivers. The wavelength of the radio emission depends on the nature of the changes in the electric field. Impulsive discharges between individual dust particles produce short wave radio emission [17], whereas large-scale fluctuations

of the electric field produce long wave radio emission [18].

Triboelectric charging of dust is also expected to be an important phenomenon on Mars. Evidence for this was the charging of the Pathfinder Sojourner Rover wheel while it operated in a martian environmental chamber [19]. Because of Mars' low atmospheric density, electrical discharges occur at lower electric potential than on Earth, and therefore should be more frequent. The breakdown electric field on Mars is expected to be between ~ 5 and 20 kV/m, compared to ~ 3000 kV/m on Earth. Electrical discharges in martian dust events would also produce wideband radio emission.

A possible explanation for the short wave radio emission by dust events is discussed next. Charges are exchanged during collisions between individual sand and/or dust particles. As the charged particles move away from each other, the electric field between them increases until it exceeds the breakdown potential, producing an impulsive discharge. This hypothesis is based on the physics of light emission by colliding ice particles proposed by Keith and Saunders [20]. The current flow associated with the impulsive discharges produce wideband electromagnetic radiation.

Several ground-based radio observations of Mars, are summarized in the next section. The observations show a strong correlation between martian dust activity and anomalously high radio emission, in wavelengths ranging from 1.35 to 6 cm. We suggest that the observed anomalous radio emissions are caused by electric activity in dust devils and dust storms, rather than thermal emission by the dusty and warmer atmosphere. Dust suspended in the atmosphere directly absorbs and scatters solar radiation, while absorbing infrared radiation, and therefore affects atmospheric heating rate and modifies the surface radiative balance [5, 21, 22]. Airborne dust produces increases in the atmospheric temperature near the top of the dust layer and decreases in the temperature at lower levels and the surface. As a result, the thermal emission by the surface and the lower atmosphere decreases, while the emission by the upper regions of the dust layer increases. Since the thermal emission at wavelengths of a few cm peaks at the surface, it is unlikely that the observed enhancement of microwave emission in regions of dust activity is of thermal origin. At radio wavelengths, scattering by atmospheric dust is insignificant, and therefore produces negligible changes in the microwave brightness temperature [23]. Hence, the thermal effect of dust is to decrease the planet's brightness temperature (see Figure 2), and any observed increase in microwave brightness must be due to non-thermal effects.

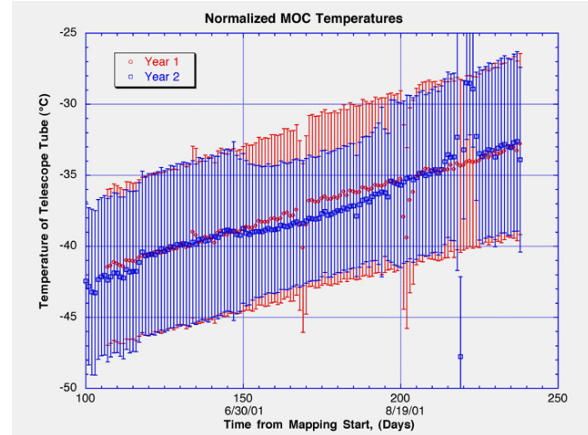


Figure 2. Temperature of the Mars Orbital Camera telescope tube during a year of weak dust storm activity (Year 1, 2000; red, lighter curve) and during a year of intense dust storm activity (Year 2, 2001; blue, darker curve). This figure is a courtesy of NASA/JPL/Malin Space Science Systems.

Radio Observations of Martian Dust Activity:

Observations of Mars at 2.8 cm with the 46 m telescope of Algonquin Radio Observatory were made in December 1975 [24, 25] and January 1978 [26]. These observations indicated that the martian disk brightness temperature was a function of the longitude of its central meridian during both set of observations. However, the brightness temperature of the longitudes ranging from 240° to 360° displayed strong variation between these two observation campaigns, and large temporal variation during the 1978 campaign. In addition, both the value of the emission and its variability are strongest in the regions of known enhanced dust activity as summarized in Figure 3. Indeed, from January to May 1978, various regional dust storms were observed in the region of anomalously high radio emission. The disk average brightness temperature observed in 1978 was so much higher than the one observed in 1975 that there were suggestions of the possibility of errors in the calibration of the two measurements [24, 25]. However, even after corrections for all probable calibration errors were done, the 1978 observations still showed significantly larger values (by more than 10 K) as shown in Figure 3. Decreases in brightness temperature might be due to cooling of the surface by dust aloft, while increases in the brightness might be due to discharges between individual dust particles.

Mars was observed with the Very Large Array (VLA) at wavelengths of 2 and 6 cm during the martian northern spring in 1983 [27]. The observations were done at the sub-earth local time of about 2 p.m., the time of largest dust devil activity. The data from

these observations exhibited behavior not well predicted by a suite of models of thermal emission. The anomalous behavior was concentrated mainly in a region of the south hemisphere bounded by the Hellas and Argyre Planitia, well known regions of large dust activity [12]. In addition, anomalous behavior was observed around the region of largest temperature gradient of the north hemisphere. This is where theoretical model predicts intense dust devils and dust storms. Indeed, Rudy et al. [27] suggested that some of the anomaly could have been caused by dust storms.

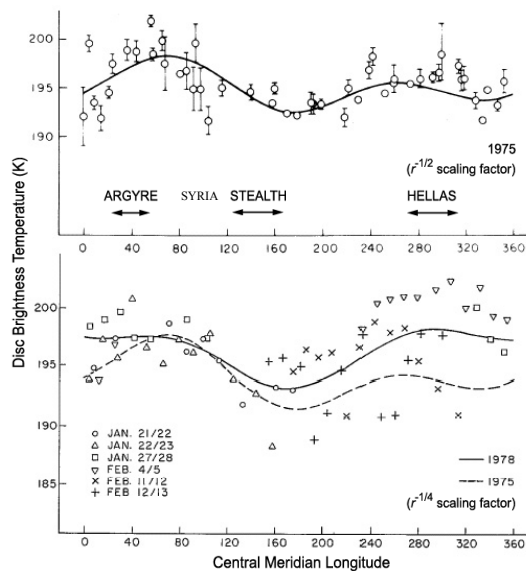


Figure 3. Measured martian disk radio brightness temperatures as a function of the central meridian longitude for 1975 (top) and 1978 (bottom) campaigns. The re-normalized brightness temperature for 1975 is also shown in the bottom plot (after [26]). Some of the most active dust devil/storm incubator regions are marked in plot at the top.

The Tharsis and Amazonis regions of Mars (referred to as the Stealth region because of its weak radar signature) were observed with the VLA at 1.35 cm during the martian northern spring in 1995 [28]. The observations of variations in surface brightness temperature of this region during a period of 12 hours were compared with theoretical predictions made with a model of the martian surface/atmosphere system. The observed anomaly (discrepancy between model and observations) in the microwave emission was found to be highest between the local noon and 4 p.m., the period in which dust devils are most frequent and strongest [2, 6]. This is also the time period in which the reduction in surface temperature by atmospheric aerosols is the highest (Figure 2). The low radar sig-

nature of the Stealth region has been attributed to the existence of loose and unconsolidated sediments such as a thick mantle of fine sand or volcanic ash [29]. The time variation of the anomalously high radio emission and the existence of large amounts of fine grains in the region are consistent with the idea that the anomalously high radio emission is caused by a large number of electrically active dust devils in the region.

Summary: The observations summarized in this article show a strong correlation between anomalously high martian microwave brightness temperature and the occurrence of dust devils and/or dust storms. We suggest that the observed anomalies are caused by impulsive discharges between dust particles, triboelectrically charged during dust events. The understanding of electrical activity associated with dust events might have important implications for the chemistry of the martian atmosphere and the safe operation of Mars landers and rovers.

References: [1] Malin et al. (1998) *Science* 279, 1681. [2] Sinclair P. C. (1973) *J. Atmos. Sci.*, 30, 1599–1619. [3] Thomas P. and Gierasch P. J. (1985) *Science*, 230, 175–177. [4] Metzger S.M. et al. (1999) *GRL*, 26, 2781–2784. [5] Gierasch P. J. and Goody R. M. (1972) *J. Atmos. Sci.*, 29, 400–402. [6] Renno N. O. et al. (1998) *J. Atmos. Sci.*, 55, 3244–3252. [7] Emanuel K. A. (1986) *J. Atmos. Sci.*, 43, 585–604. [8] Renno N. O. et al. (2000) *JGR*, 105, 1859–1865. [9] Renno N. O. and Bluestein H. B. (2001) *J. Atmos. Sci.*, 58, 927–932. [10] Cantor B. A. et al. (2001) *JGR*, 106E10, 23,653–23,687. [11] Cantor B. A. et al. (2002) *JGR*, 107E3, 101,029–101,036. [12] Kieffer H. H. et al. (1992) *Mars*, Univ. Arizona Press. [13] Krauss C. E. et al. (2002) *AGU 83(47)*, Fall Abstract P51A-0338. [14] Delory G. T et al. (2002) *AGU 83(47)*, Fall Abstract P51A-0335. [15] Towner M. C. et al. (2002) *AGU 83(47)*, Fall Abstract P51A-0342. [16] Ette A. I. I. (1971) *J. Atmos. Terr. Phys.*, 33, 295. [17] Wilson J. (2002) personal comm. [18] Farrell W. et al. (2002) *AGU 83(47)*, Fall Abstract P51A-0336. [19] Ferguson D. C. et al. (1999) *JGR*, 104E4, 8747–8759. [20] Keith W. D. and Saunders C. P. R. (1988) *Nature*, 336–364, 362. [21] Zurek R. W. (1978) *Icarus*, 35, 196–208. [22] Davies D. W. (1979) *JGR*, 84, 8289–8293. [23] Paltridge G. W. and Platt C. M. R. (1976) *Radiative Processes in Meteorology and Climatology*, Chap. 9, Elsevier. [24] Andrew B. H. et al. (1977) *ApJ*, 213, L131–134. [25] Andrew B. H. et al. (1978) *ApJ*, 220, L61. [26] Doherty L. H. (1979) *ApJ*, 233, L165–L168. [27] Rudy D. J. et al. (1987) *Icarus*, 71, 159–177. [28] Ivanov A. B. et al. (1998) *Icarus*, 133, 163–173. [29] Muhleman D. O. et al. (1991) *Science*, 253, 1508–1513.

THE PLANETARY UNDERGROUND TOOL (PLUTO) EXPERIMENT ON THE BEAGLE 2 MARS LANDER.

L. Richter¹, V.V. Gromov², H. Kochan¹, K. Kosacki³, and T. Tokano¹. ¹DLR Institute of Space Simulation, Linder Hoehe, D-51170 Cologne, Germany (lutz.richter@dlr.de), ²VNIITransmash, 2 Zarechnaja Ul., 198323 St. Petersburg, Russia (tm@mvei.ru), ³Warsaw University, Institute of Geophysics, Warsaw, Poland (kjkosac@fuw.edu.pl).

Introduction: The payload of the Beagle 2 Mars lander of ESA's Mars Express mission includes a regolith-penetrating, tethered "Mole" intended for acquisition of several subsurface soil samples from depths between about 10 cm and approximately 1.5 m. These samples will then be analysed by the Gas Analysis Package (GAP) instrument on the lander, primarily with regard to isotopic composition and organic molecules [1]. In addition, a share of each sample can be deposited onto the lander structure to be investigated with instruments mounted on the lander's PAW instrument carrier, such as the Mossbauer and X-ray fluorescence spectrometers and the optical microscope. After giving a brief overview of the experiment design, this paper focuses on the various science objectives addressed by the Beagle 2 Mole system, also referred to as the PLanetary Underground TOol (PLUTO). Apart from its capability to make subsurface regolith samples available to lander-based experiments for the first time on a Mars landing mission, PLUTO will be capable of performing scientific measurements of its own which utilize the Mole's soil penetration process and its temporary residence within the regolith.

PLUTO Overview: The PLUTO instrument on the Beagle 2 Mars lander, scheduled to arrive at Mars on December 25 this year, has at its core an electromechanical "Mole" that is able to penetrate into soil-like materials by way of soil displacement through an internal hammering mechanism that transfers periodic force strokes from the Mole to its outside environment [2]. In the presence of friction with the surrounding material, a self-penetration without requiring reactive forces from the lander is possible, allowing to link the Mole to lander-based elements through a tether which also serves as the primary means of retrieving the device. Hammer mechanism sizing allows to advance to depths of about 1.5 m in Viking-type "blocky" soil with an assumed hyperbolic increase of bulk density and shear strength with depth, within about 2 h of continuous hammering while at Martian gravity, with average electrical power uptake of roughly 3 W. A sampling mechanism in the front of the Mole can be commanded to open to capture a soil sample between about 5 mm³ and 200 mm³, depending on sampler operating scheme. A winch mechanism residing above the surface will allow to reel the Mole back inside a "holster"-like guiding tube – supported by Mole backwards hammering - which is maneuvered by the lander mechanical

arm to allow sample discharge to either the sample inlet of the Gas Analysis Package (GAP) instrument or onto the lander deck. In all, three subsurface sample acquisitions from the Martian regolith are planned during the course of the mission within reach of the lander arm, from various depths not exceeding about 2 m. Overall mass of PLUTO including winch mechanism and tether is 860 g at a stowed length of 365 mm.



Fig. 1: Beagle 2 in deployed configuration on surface of Mars (artist's impression).

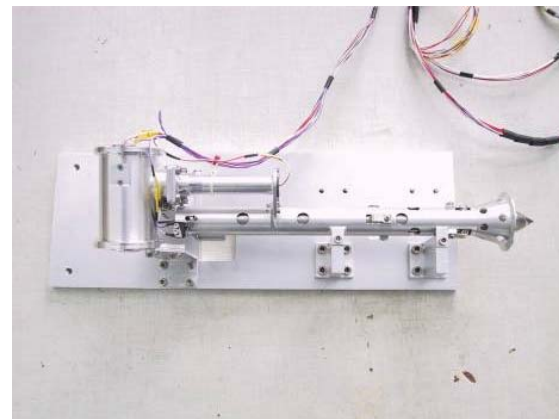


Fig. 2: PLUTO Qualification Model (with winch reel mechanism and guiding tube).

Subsurface Sample Analyses: The lander-based GAP instrument, using pyrolysis and stepped combustion processes, aims at studying the retrieved subsurface soil samples in light of a search for organic molecules either imported by carbonaceous meteorites or perhaps produced on Mars by non-biological or even

biological processes [3]. Access to subsurface soil for this type of investigation is considered essential to account for Mars soil oxidant hypotheses as well as decomposition processes driven by solar UV alone [4], [5]. Moreover, analyses of subsurface soil samples by the Beagle 2 Mossbauer spectrometer after sample deposition on the lander structure offer the potential to directly investigate oxidation state as a function of sample provenance (depth). GAP additionally will be able to measure water released from samples during pyrolysis, allowing to differentiate between chemically bound and adsorbed water [6] while delivering ground truth for the Mars Odyssey GRS suite measurements of soil hydrogen abundance.

Soil Mechanics: The PLUTO Mole will allow mechanical properties of the regolith to be inferred from the way it proceeds into the Martian soil. Using a Mole soil penetration theory calibrated by ground-based experiments, regolith bulk density, cohesion, and internal friction angle can be constrained as a function of depth using the Mole penetration path (and retrieval path) vs. time which is measured by a sensor indicating the amount of tether extracted by the Mole. The obtained depth profiles of these quantities should provide insight into the depositional history and stratigraphy of the regolith at the site by uncovering any layering of soils with different mechanical properties being indicative of the upper horizons of the local geological sequence. It is expected that absolute values derived for cohesion will be accurate to within 100 Pa, and for friction angle to within 3° .

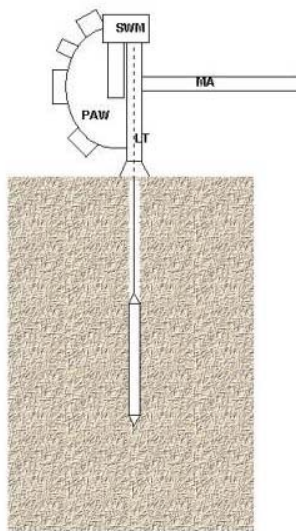


Fig. 3: Schematics of Mole downward deployment from the PAW instrument carrier at end of Beagle 2 mechanical arm.

Thermophysical Properties: A temperature sensor mounted on the Mole will support investigations of soil thermophysical properties and measurements of the subsurface temperature profile. Regolith temperature measurements will be conducted both as a function of depth during soil intrusion and retrievals, and as a function of time for constant depth, as the Mole can be left in the subsurface for periods of days before it is retrieved, especially during the later part of the Beagle 2 landed mission. Subsurface temperature data will support calibrations of Mars regolith thermophysical models, especially if coupled with thermal measurements conducted concurrently above the surface by sensors on the lander itself. Once soil thermal diffusivity is derived from the data, this can be solved for soil effective thermal conductivity using the bulk density estimates obtained from the PLUTO soil mechanics investigation, allowing in turn an estimate of the soil grain size regime from known correlations between thermal conductivity and grain size [7].

Volatile Condensations from Atmosphere: Provided the boreholes created by Mole soil penetration remain stable following retrieval of the device back to the surface, a search for condensed atmospheric volatiles along permanently shaded borehole walls will be conducted by periodic imaging with one of the lander camera heads being equipped with an illuminating torch. This will allow an independent estimate of the soil thermal conductivity to be derived, and would enable to constrain atmospheric water vapor content, utilizing simultaneous measurements of atmospheric pressure and temperature by sensors on the lander.

References: [1] Sims M.R., et al. (1999) *Instruments, Methods, and Missions for Astrobiology II*, Proc. Internat. Soc. for Opt. Engng., Proc. Series, 3755, pp. 10-23. [2] Richter L. et al. (2002) *Planetary and Space Science* 50, pp. 903-913. [3] Morgan, G. et al. (2003) *EGS XXVIII*. [4] Klein H.P. (1978) *Icarus* 34, pp. 666-674. [5] Stoker C.R., and Bullock M.A. (1997) *JGR* 102 E5, pp. 10,881-10,888. [6] Tokano T. and Richter L., *Icarus*, submitted. [7] Presley M.A., and Christensen P.R. (1997). *JGR* 102 E4, pp. 9,221-9,229.

VIKING LANDER 1 AND 2 REVISITED: THE CHARACTERISATION AND DETECTION OF MARTIAN DUST DEVILS. T. J. Ringrose, M. C. Towner and J. C. Zarnecki, Planetary and Space Sciences Research Institute, The Open University, Walton Hall, Milton Keynes, MK7 6AA, UK, t.j.ringrose@open.ac.uk.

Introduction: During the summer of 1976 Viking Lander 1 and 2 touched down at Chryse Planitia and Utopia Planitia, Mars respectively. The primary aim of both Viking Landers was to look for the presence of organic life on the surface of Mars, however each Lander also had a comprehensive meteorological package to monitor the martian atmospheric conditions [1]. The meteorological package consisted of pressure, temperature and wind sensors, enabling the landers to perform the first detailed in-situ investigation of martian weather. Data was logged for the full mission at a variety of sampling rates. High data rates were used early on in the mission (one sample every 8 seconds), but this moved to a lower rate (one sample per minute) after sol 60 for Viking Lander 2. The meteorological results from the Viking Landers highlighted diurnal variations in pressure and temperature. The ambient wind speeds were generally below 10ms^{-1} . The biggest pressure variation was between the two landing sites; explained by the difference in latitude and altitude. Apart from this variation the long-term pressure was relatively constant at approximately 6 mbar. Large temperature variations were seen to be commonplace on Mars, with a diurnal range of approximately 50K. This diurnal temperature variation is essentially a consequence of the low thermal inertia of the surface and the atmosphere.

Dust devils form at the base of convective plumes. These convective plumes are created by surface heating from the Sun. Dust devils, when detected, will produce changes in all of the key meteorological parameters measured by the Viking Landers, namely pressure, temperature, and wind. These vortices may also leave tracks or marks on the surface where they have lofted the surface regolith; these were first seen and identified from Viking orbital photography [2]. The two Viking Lander meteorological instruments did indeed detect possible convective vortices, first reported by Ryan and Lucich, (1983), who gave an indication of annual occurrence statistics. Mars Pathfinder also detected 79 convective vortices inferred from pressure variations [3]. Dust devils have also been detected in some of the Mars Pathfinder wide angle camera images [4]. It is clear therefore that dust devils occur on Mars, and their relevance to the martian global dust cycle is currently a topic of scientific interest [4-6].

Vortex Detection: Convective vortices can be detected by a characteristic behaviour in their meteorological parameters. This signature or change in mete-

orological parameters could include a change in wind speed and direction, a rise in temperature, or a drop in pressure. The last two parameters will only be truly characteristic if the sensor suite encounters the vortex core.

Modelling exists to approximate empirically the wind speed and direction changes characteristic of atmospheric vortices. Wind speed is modelled using the Rankine vortex method [7], where the tangential wind speed decreases with a $\frac{1}{r}$ relationship from the edge of the core boundary outwards to the edge of the zone of influence (approximately 10 x visible core radius) and also decreases linearly inwards to zero at the centre of the vortex. Apparent wind direction (as seen by a stationary observer) is calculated using simple trigonometry. The modelled vortex signature can then be used to identify vortices in meteorological data.

To identify convective vortices from the Viking Lander meteorological data, the detection technique used is to compare a time-averaged mean to a threshold value, commonly known as a phase picker. For each variable under consideration, this method calculates a short term mean, STA (a running average of the last few readings), and a long term mean, LTA (a running average covering a longer period of time). The difference between the STA and LTA is compared to a specified threshold value. (values of 6ms^{-1} for wind speed and 40 degrees for wind direction in this study).

$$|STA - LTA| > \text{threshold} \quad (1)$$

The STA uses for example the most recent 3 samples and the LTA uses the most recent 50 samples (dependent on sample rate). This approach is widely used in seismology for time series data to detect events of interest [8]. Possible convective vortex events are then highlighted and examined manually. The technique not only picks out possible convective vortices but will trigger on other anomalies in the data such as gradients in the wind data which are also of interest. This method has been used successfully to detect terrestrial dust devils during a recent field investigation, as part of the MATADOR 2001 programme [9].

Classification of Convective Vortex Events: Once the dust devil is detected a Rankine fit can be used to estimate miss distance and diameter to give a better picture of the vortex. In addition the meteorological phenomena seen by The Viking Landers convective vortices have been classified, allowing for easy

identification of convective vortices. This classification gives a clear indication of what to look for in a possible dust devil event. This classification is not intended to be specific to Viking and could be used to classify convective vortices from any field study, including future missions. Convective vortices are divided into three groups, core (1), near miss (2), and possible (3). The first two categories are then subdivided to differentiate between convective vortices and dust devil events. Category 3 is reserved for 'possible events', which pass a considerable distance from the sensors and may or may not fit the empirical Rankine vortex model. Two further categories 4 and 5 describe sustained gusts, and other transient events that do not fit into other categories.

Results: Ryan and Lucich (1983) analysed a total of 129 (Viking Lander 1) and 151 sols (Viking Lander 2) of which 43% and 39% contained vortices respectively. They also provided seasonal statistics on the formation of vortices. The analysis contained in this paper does not cover the seasonal variation which was analysed by Ryan and Lucich, but provides a more in depth analysis of diurnal statistics for the Viking landers, which will complement the findings of Ryan and Lucich.

The threshold values used produced 38 possible vortices in the first 60 sols of Viking Lander 2 [with STA = 3, LTA=50, and a sample rate of 0.5 to 0.0625 Hz]. These candidates were then manually confirmed by looking at the pressure and temperature variations. This number of vortex events is consistent with the statistics from previous martian dust devil studies of the Viking Landers [10]. 34 other events were detected for Viking Lander 2 ranging from direct passes over the meteorological sensors to gusts or unidentifiable events. The entire data set was also scanned by eye to confirm the efficiency of the phase picker algorithm used. Events were then classified according to the scheme described previously.

It is believed that some true dust devils have been detected, defined as a convective vortex with wind speeds above the threshold wind speed able to loft sand particles, ($25\text{-}30\text{ms}^{-1}$, [11]). However there is no way to be sure if these did in fact loft surface particles. Recent work is tending to indicate that dust devils may not follow traditional saltation rules [5]. During the martian summer of 1976 the wind speeds were in general below 10ms^{-1} , which would be insufficient to loft surface particles by traditional methods.

Of the 38 possible vortices, an initial analysis indicated no preference between clockwise and counter-clockwise rotation, in agreement with Ryan and Lucich(1983).

Diurnal Statistics: Considering the diurnal occurrence and properties of the martian wind dominated phenomena detected, Fig. 1 summarises the diurnal statistics for categories 1, 2, and 3, (possible convective vortices for Viking Lander 2 sols 1-60) and shows a maximum at between 13:00 and 13:30, with the majority of activity happening before this time. This is similar, but not exactly the same behaviour, to that seen on Earth, where the maximum generally comes in the afternoon, with little activity in the morning.

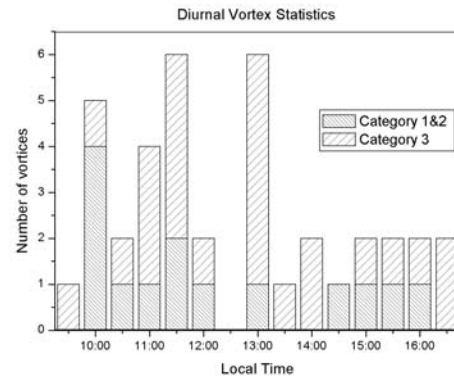


Figure 1 Diurnal statistics for vortices seen by VL2

Classification Example: Figure 2 a convective vortex (category 1b) from sol 4 (Viking Lander 2), which has a distinctive vortex signature. There is an abrupt shift and return to ambient in wind direction, a peak in wind speed and temperature, all in a time scale of about 90 seconds. This is a good example, showing the vortex core, and the convective vortex must have passed almost directly over the lander.

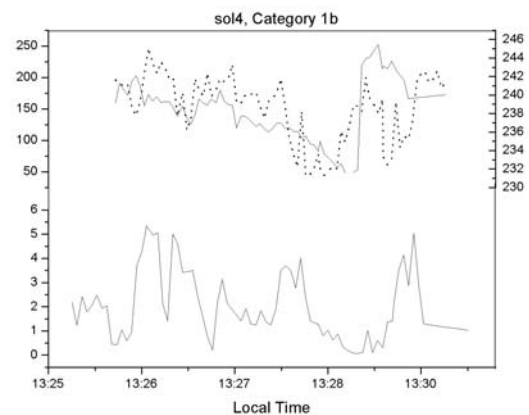


Figure 2 The upper solid line and upper left axis represents wind direction in degrees, from the local north, the lower solid line and lower left axis is wind speed (ms^{-1}), the short dashed line is temperature (K), upper right axis.

Implications: At the Mars Pathfinder landing site the dust deposition rate was estimated to be $5\text{-}15 \mu\text{m yr}^{-1}$. This would result in a surface particulate layer metres thick accumulating over a geologically short period of time, suggesting that large amounts of surface material is constantly redistributed around the surface [12]. Applying the estimates of dust loading of appropriate dust devils seen by the Mars Pathfinder [4] to the Viking data, one can estimate the total amount of surface material lofted by dust devil events around Viking Lander 2 over the first 60 sols to be at least 3.4×10^4 kg, equivalent to $800 \pm 10 \text{ kgsol}^{-1} \text{ km}^{-2}$. This assumes a dust loading of $7 \times 10^{-5} \text{ kg m}^{-3}$, an average vertical velocity of 7 ms^{-1} and a dust free core of 50% [13, 14]. This strongly implies that dust devils are responsible for redistributing large amounts of martian surface material over a geologically short time period.

Conclusions: Convective vortices and dust devils have been seen on Mars both in orbital data and meteorological data, as well as lander images. Previous estimates of dust devil activity [10] at the Viking Lander sites have provided information about the seasonal behaviour. To add to this data set, Viking Lander 2 meteorological data has been analysed for the sols 1-60, which have a sufficiently high sampling rate for reliable detection of short-term meteorological phenomena. Convective vortices have been identified from their distinctive meteorological signature, using a phase picker algorithm [8] and categorized by a rating scheme, which considers intensity and confidence of detection. Wherever possible, estimates are made of the core miss distance from the Lander and the predicted diameter of the vortex, assuming a response for the vertical sensitivity of the wind sensor, and estimating a vertical wind profile within a convective vortex based on previous studies. An estimate of maximum wind speed within the vortex is also made and compared to the estimated dust saltation threshold at the landing site [15] to infer if the vortex was dust laden. In total, over the 60 sols of Viking Lander 2, 38 vortices have been detected. It is thought that a few of these vortices are false signals due to lander body interference [1] but 6 of the 38 have sufficient wind speeds to entrain local surface material from the landing site. Diurnal activity is similar to terrestrial behaviour, but with increased early morning activity, which it is inferred is probably due to a lower adiabatic lapse on Mars. Total number statistics seen here give a detection rate of 0.6 vortices per sol, compared to recent results of 2 per sol seen by Mars Pathfinder [3]. These results illustrate how common convective vortices are on Mars and potentially how important dust devils are in shaping the martian surface. As a broad estimate, applying the Mars Pathfinder estimates of dust devil

dust loading, the total amount of material lofted in the area of the Viking Lander 2 is of the order of $800 \text{ kgsol}^{-1} \text{ km}^{-2}$. This analysis is in agreement with the earlier study by Ryan and Lucich and adds to the published data by providing data on the diurnal behaviour of convective vortices at the Viking 2 landing site. Further analysis is currently ongoing characterizing convective vortex events from the Viking Lander 1 data.

References: [1] Hess, S., et al., *Meteorological results from the surface of Mars: Viking 1 & 2*. JGR., 1977. **82**: p. 4559-4574. [2] Thomas, P. and P. Gierasch, *Dust Devils On Mars*. Science, 1985. **230**: p. 175-177. [3] Murphy, J.R. and S. Nelli, *Mars Pathfinder convective vortices: Frequency of occurrence*. GRL, 2002. **29**(23). [4] Metzger, S. and M. Carr, *Dust devil Vortices seen by the Mars Pathfinder Camera*. GRL, 1999. **26**: p. 2781-2784. [5] Balme, M., et al. *Dust devils on Mars: results from threshold test using a vortex generator*. in LPSC. 2002. [6] Tratt, D., et al. *In Situ Measurements of Dust Devil Dynamics*. in *American Geophysical Union*. 2001. [7] Faber, T.E., *Fluid Dynamics for Physicists*. 1995: Cambridge University Press. [8] Allen, R., *Automatic Phase Pickers: Their Present Use and Future Prospects*. Bulletin of the Seismological Society of America, 1982. **72**(6): p. 225-242. [9] Hecht, M., et al., *MATADOR Dust Devil Campaign*. 2001. [10] Ryan, J. and R. Lucich, *Possible Dust Devils, Vortices on Mars*. JGR., 1983. **88**: p. 11005-11011. [11] Greeley, R. and J.D. Iversen, *Wind as a geological process on Earth, Mars, Venus, and Titan*. 1985: Cambridge University Press. [12] Golombek, M.P. and N.T. Bridges, *Erosion rates on Mars and implications for climate change: constraints from the Mars Pathfinder Landing site*. JGR., 2000. **105**: p. 1841-1853. [13] Metzger, S., *Dust Devils as Aeolian Transport Mechanisms in Southern Nevada and the Mars Pathfinder Landing Site*, in *Department of Geology*. 1999, Ph.D., University of Nevada: Reno. p. 208. [14] Sinclair, P., *A Quantitative Analysis of The Dust Devil*, in *Geology*. 1966, Arizona State. [15] Greeley, R., et al., *Threshold Windspeeds for Sand on Mars: Wind Tunnel Simulations*, GRL, 1980. **7**: p. 121-124.

Acknowledgements: Jim Murphy (New Mexico State University) is thanked for providing the Viking Lander meteorological data. David Tratt (Jet Propulsion Laboratory) is thanked for kindly providing access to the MATADOR wind data. We greatly appreciated valuable revisions from two anonymous reviewers.

BASALTIC ANDESITE OR WEATHERED BASALT: A NEW ASSESSMENT. S. W. Ruff¹, ¹ Department of Geological Sciences, Arizona State University, Tempe, AZ 85287-6305, ruff@tes.asu.edu.

Introduction: One of the most significant results to emerge from the Mars Global Surveyor Thermal Emission Spectrometer (TES) is the observation of two distinct thermal infrared (TIR) spectral units in the low albedo regions of Mars [1]. One of these units has the spectral characteristics of a plagioclase- and pyroxene-rich flood basalt and is found mostly in the southern highlands (Syrtis-type). The second unit, which is concentrated in the northern lowlands but is distributed across the highlands as well, has been characterized as a plagioclase- and glass-rich basaltic andesite (Acidalia-type). While the basaltic identification for the Syrtis-type spectrum is accepted widely, the andesitic characterization of the Acidalia-type spectrum is the source of considerable debate. One reason for this debate is the argument that the production of voluminous andesite requires plate-tectonic subduction [2], which is lacking on Mars. Several alternative hypotheses have been presented to explain the apparent andesitic character of the Acidalia-type spectrum. These include: oxidation and recrystallization of a SNC-type basalt [3]; weathering of basalt to produce clay minerals [2]; silica coating on basalt [4]; and palagonitization of basalt [5]. In all of these cases it has been shown that alteration of a precursor basalt can yield a spectrum that resembles the Acidalia-type spectrum. While such explanations dispense with the idea of large volumes of basaltic andesite on Mars, they require a process by which some of the basaltic materials on Mars become altered while some remain relatively pristine.

The basis for the ambiguity in the basaltic andesite identification lies in the fact that mineral glasses, both volcanic or authigenic, and some clay minerals have significant spectral overlap in the TIR wavelengths [2]. Recently it has been shown that some zeolites [6] and palagonites [5] also have overlapping spectral features. While it may be impossible to differentiate unambiguously between some of these candidates because their spectral differences are so subtle, in other cases it may be more feasible. As was noted by [2] and [6], some of the candidate clay minerals for Mars have distinctive spectral characteristics in a portion of the TIR spectrum that has been excluded in atmospherically-corrected TES spectra because of the absorption of atmospheric CO₂. The excluded region is wider than necessary in an effort to avoid the confounding effects of CO₂. However, CO₂ opacity remains relatively low in the region of the critical distinguishing features between clay minerals and glasses. Careful scrutiny of non-atmospherically-corrected TES spectra may serve

to distinguish between the two. This work presents an initial assessment of whether montmorillonite and some other clay minerals are present on the martian surface. While such work is not sufficient to settle the andesite debate, it does shed light on the viability of some of the alternative hypotheses.

Spectral Details: The Syrtis- and Acidalia-type spectra identified by [1] are shown in Figure 1. It is clear that the Acidalia-type spectrum has fewer spectral features than the Syrtis-type spectrum, which is part of the reason it lacks an unambiguous lithological identification.

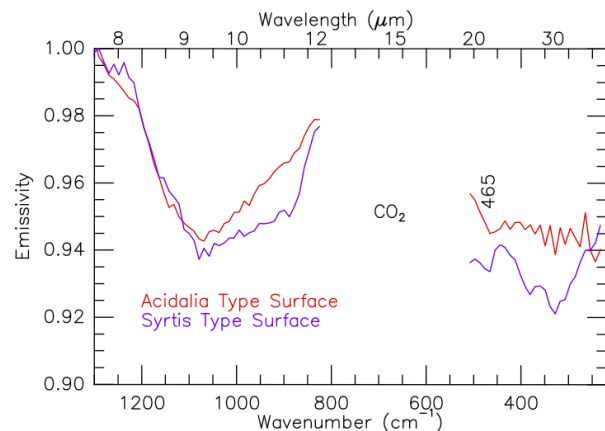


Figure 1. The two volcanic-unit spectral classes identified by [1]. The 465 cm⁻¹ feature is described in the text.

Figure 2 shows the Acidalia-type spectrum along with a set of laboratory spectra of candidate materials with similar spectral characteristics. The common features are the prominent V-shape centered at ~1100 cm⁻¹ and a secondary feature centered at ~465 cm⁻¹. The montmorillonite spectrum has an additional feature at ~530 cm⁻¹ that readily distinguishes it from the glass and zeolite spectra. However, this feature is within the CO₂ exclusion region of the atmospherically-corrected TES spectrum and thus is not available for spectral deconvolution analysis. As shown by a typical non-atmospherically-corrected TES spectrum (Figure 3), in the region between the current lower limit of CO₂ exclusion at 508 cm⁻¹ and 560 cm⁻¹, the absorption by CO₂ is limited to a “hot band” at ~545 cm⁻¹. The strong absorption of surface radiance by atmospheric CO₂ begins at wavenumbers > 560. Because of this, the presence of a spectral feature attributable to clay minerals should be discernable in TES spectra.

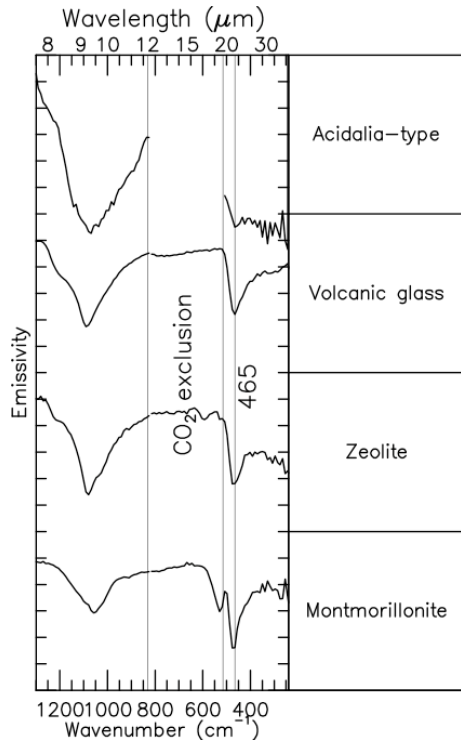


Figure 2. Mars Acidalia-type spectrum compared with candidate materials of similar spectral character.

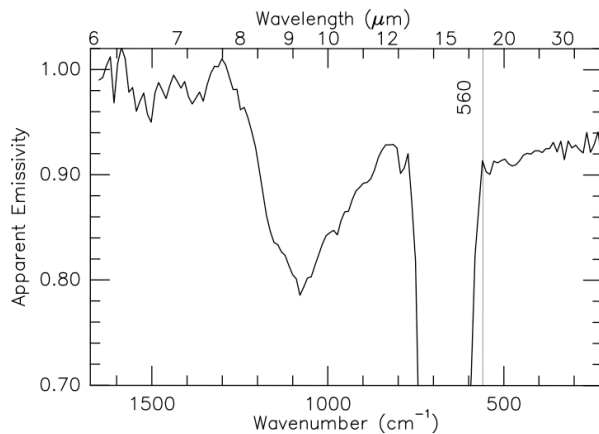


Figure 3. Non-atmospherically-corrected average spectrum of southern Acidalia. Atmospheric CO₂ absorption does not become significant until > 560 cm⁻¹.

Searching for Clay Minerals: A series of candidate clay mineral spectra is shown in Figure 4. In an effort to match the general spectral characteristics of the Acidalia-type spectrum, these laboratory spectra were selected based on the presence of a V-shaped feature in 1100 cm⁻¹ region and a second feature at ~465 cm⁻¹. The latter feature is especially important because it serves as a proxy for the identification of Acidalia-type spectral regions on Mars. This is shown in Figure 5b which represents a global map of a spec-

tral index developed to identify the ~465 cm⁻¹ feature in non-atmospherically-corrected TES spectra. For comparison, the “andesite” map of [1] also is shown (Fig. 5a). From this comparison it can be seen that the ~465 cm⁻¹ feature maps out the same regions of Acidalia-type spectral character as does the spectral deconvolution technique employed by [1] but with the benefit of improved signal to noise. An obvious mismatch is the inclusion of the hematite-rich locations at Meridiani Planum and Aram Chaos in the index map. This is due to the overlap of a hematite spectral feature in the same spectral region as the index.

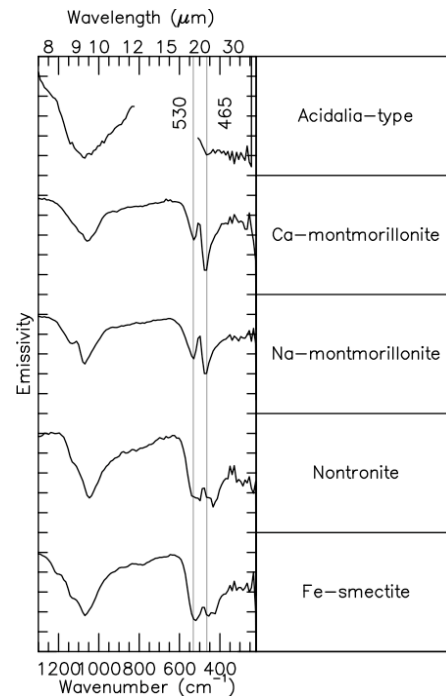


Figure 4. Candidate clay mineral spectra compared with Acidalia-type spectrum.

Because of the significance of the ~465 cm⁻¹ feature as related to the Acidalia-type spectral unit, it is reasonable to conclude that at least one of the components of Acidalia-type material has a prominent feature in this location. As shown by Figure 2, glass and zeolite have such a feature as does montmorillonite and to a lesser extent, nontronite and Fe-smectite (Figure 4). Each of these clay minerals also has a second absorption feature at ~530 cm⁻¹ separated from the ~465 cm⁻¹ feature by an emissivity peak. The ~530cm⁻¹ feature falls within the CO₂ exclusion region instituted by [1] but well outside of any significant CO₂ absorption. Therefore it should be discernable in non-atmospherically-corrected TES spectra. An index for this feature has been developed and a global map of the index is shown in Figure 5c.

Results: The combination of the index maps defined in the previous section is a necessary but not sufficient strategy to identify certain clay minerals on the surface of Mars. A positive correlation between the two indices would be good evidence for these clay minerals. As can be seen by comparing the two maps in Figure 5, the northern lowland occurrences of the Acidalia-type spectral unit are not matched by the $\sim 530\text{ cm}^{-1}$ feature index. Instead, this index maps out portions of Syrtis Major, Terra Cimmerium, and other highland, low albedo regions. This distribution is attributable to a feature in Mg-rich olivine that overlaps that of the clay minerals used to define the index. For example, the prominent region of high $\sim 530\text{ cm}^{-1}$ index values in the location of Nili Fossae (NE Syrtis Major) coincides with a known olivine anomaly [7, 8]. The two hematite locales also are identified with this index because of an overlapping spectral feature in hematite.

Conclusions: Volcanic glass and some zeolites and clay minerals are viable components of the Acidalia-type material. A spectral feature at $\sim 465\text{ cm}^{-1}$ is common to all three candidates and the Acidalia-type spectrum. An index developed to identify this feature in non-atmospherically-corrected TES spectra readily distinguishes Acidalia-type spectral units from Syrtis-type. A second feature at $\sim 530\text{ cm}^{-1}$ is present in some candidate clay minerals and has the potential to be used to distinguish clay minerals from zeolites and glass. An index developed to identify this feature in non-atmospherically-corrected TES spectra shows no correlation with the index of the $\sim 465\text{ cm}^{-1}$ feature, diminishing the likelihood of the presence of certain clay minerals in the Acidalia-type material. This weakens the case for weathered basalt as an alternative to andesite in the northern lowlands of Mars. However, because zeolite can form as the result of weathering processes [e.g., 9, 10] and its spectral character can be so similar to volcanic glass, it may be that weathering or alteration of basalt has produced zeolites rather than clay minerals.

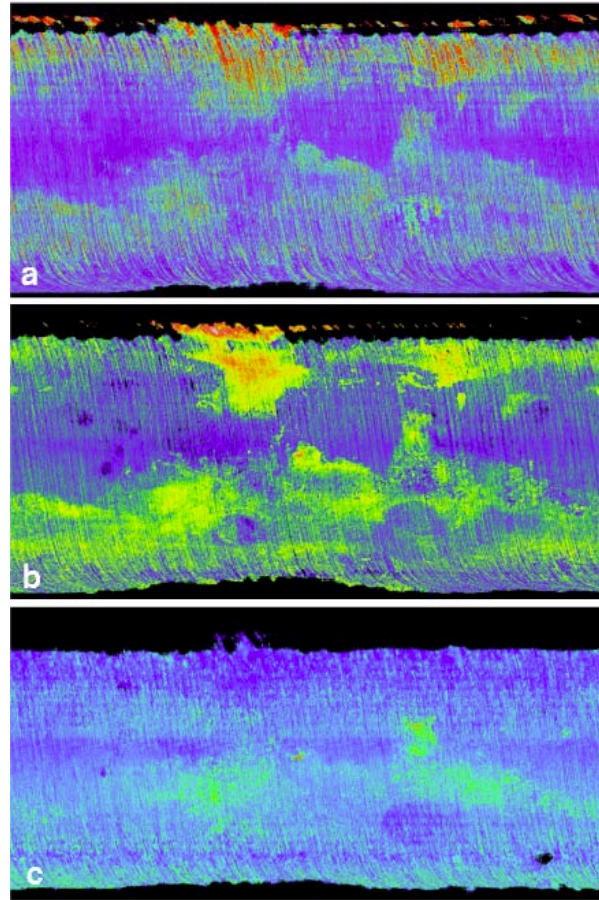


Figure 5. Global maps of TES spectral data. (a) andesite abundance map of [1]; (b) spectral index representing the feature at $\sim 465\text{ cm}^{-1}$ in the Acidalia-type spectrum; (c) spectral index representing a feature at $\sim 530\text{ cm}^{-1}$ found in some clay minerals, olivine, and hematite.

References: [1] Bandfield J. L., V. E. Hamilton and P. R. Christensen (2000) *Science*, 287, 1626-1630. [2] Wyatt M. B. and H. Y. McSween, Jr (2002) *Nature*, 417, 263-266. [3] Minitti M. E., J. F. Mustard and M. J. Rutherford (2002) *J. Geophys. Res.*, 107(E5), doi: 10.1029/2001JE001518. [4] Kraft M. D., T. G. Sharp and J. R. Michalski (2003) *Lunar Planet. Sci.*, XXXIV, abstract 1420. [5] Morris R. V., T. G. Graff, S. A. Mertzman, M. D. Lane and P. R. Christensen (2003) *Lunar Planet. Sci.*, XXXIV, abstract 1874. [6] Ruff S. W. and P. R. Christensen (2003) *Lunar Planet. Sci.*, XXXIV, abstract #2068. [7] Hoefen T. M., R. N. Clark, J. C. Pearl and M. D. Smith (2000) *Bull. Am. Astro. Soc.*, 32, 1118. [8] Hamilton V. E. and P. R. Christensen (2003) *Lunar Planet. Sci.*, XXXIV, abstract 1982. [9] Allen C. C., J. L. Gooding, M. Jercinovic and K. Keil (1981) *Icarus*, 45, 347-369. [10] Dickinson W. W. and M. R. Rosen (2003) *Geology*, 31, 199-202.

EVOLUTION OF VOLATILE-RICH CRATER INTERIOR DEPOSITS ON MARS. Patrick S. Russell¹, James W. Head¹, Michael H. Hecht², ¹Department Geological Sciences, Brown Univ., Providence, RI 02912 USA, ²Jet Propulsion Laboratory, Pasadena, CA, USA. Patrick_Russell@Brown.edu.

Introduction: Many craters on Mars are partially filled by material emplaced by post-impact processes. Populations of such craters include those in the circum-south polar cap region, in Arabia Terra, associated with the Medusae Fossae Formation, and in the northern lowlands proximal to the north polar cap. In this study, crater fill material refers to an interior mound which is generally separated from the interior walls of the crater by a trough that may be continuous along the crater's circumference (i.e. a ring-shaped trough), or which may only partially contact the crater walls (i.e. a crescent-shaped trough). The fill deposit is frequently off-center from the crater center and may be asymmetric, (i.e. not circular) in plan view shape.

Such craters associated with the Medusae Fossae Formation are likely partially exhumed and contain remnants of Medusae Fossae material that may be ignimbrites [1], eolian materials [2, 3], true polar wander deposits [2], volatile-rich deposits [4], or volcanic ash accumulation [5]. In Arabia, such crater fill has also been interpreted as polar layered deposits associated with true polar wander [2] or lacustrine sedimentary deposits [6]. The fill of craters around the south pole is contiguous with south polar layered material, which argues for a similar process of deposition [7] with possible later exhumation of or flow into the crater [8]. Two craters at high northern latitudes contain fill material but are well separated from the north polar layered terrain: Korolev (73°N, 195°W; Fig. 1) and an unnamed crater (77°N, 145°W). This configuration suggests this fill material was also deposited in a similar manner to the polar cap materials [7] and may or may not be remnants of a formerly more extensive polar cap [9].

Motivated by assessment of the martian hydrological cycle, especially the groundwater system, we have previously examined northern lowlands craters for signs that the associated impacts may have interacted with the groundwater system [10,11]. Given the physical and thermal disruption of the ground associated with impact, disruption of the subsurface cryosphere could have allowed effusion of sub-cryosphere confined groundwater into the crater under artesian-like conditions [10,12]. In a globally interconnected hydro-sphere-cryosphere system [12], this process would be favored in the northern lowlands due low planetary elevation, where hydraulic pressure head of the groundwater system should be greatest [11]. Such a scenario presents an alternative hypothesis for volatile-rich crater fill in northern lowlands craters. However, the only large craters in the northern lowlands containing significant fill material are most proximal to the north polar cap [11]. Unless these impacts were

very recent, such that the volatile fill had not yet sublimated away [13], this non-random clustering near the pole suggests polar-like processes are more likely responsible for their formation. By the same argument of higher hydraulic heads at lower surface elevations in a global groundwater system, impacts into high-elevation circum-south polar terrain would not be expected to have accessed subsurface water. Remaining favored hypotheses of formation of circum-polar crater fill material include preferential deposition by polar-like processes in isolated craters, or deposition contiguous with, or part of, a formerly more extensive polar cap [e.g., 9] by processes identical to those that formed the polar cap. Given these theories of crater fill formation by deposition from above, fill material in the north and south polar regions is almost certainly rich in volatiles, and even the fill of equatorial craters may contain significant volatiles.

Volatile-rich deposits have the property of being modifiable by the local stability of the solid volatile, which is governed by local energy balance. Here we test the hypothesis that asymmetries in volatile fill shape, profile, and center-location within a crater result from asymmetries in local energy balance within the crater, due mainly to variation of solar insolation and radiative effects of the crater walls over the crater interior. We first focus on Korolev crater [14] in the northern lowlands. We then apply this model to other craters in different regions. If asymmetry in morphology and location of crater fill are consistent with radiative-dominated asymmetries in energy budget within the crater, then 1) the volatile-rich composition of the fill is supported (this process should not be effective at shaping volcanic or sedimentary deposits), and 2) the dominant factor determining the observed shape of volatile-rich crater fill is the local radiative energy budget within the crater (and erosive processes such as eolian deflation are not necessary).

We also use a geographic and energy model approach to specifically test the idea that material in partially filled craters around the south pole may once have been contiguous to the cap and may have been sustained and modified by radiative processes specific to the crater environment (as opposed to the surrounding plains) as the cap retreated.

Korolev Crater: Korolev crater (~80 km diameter) is superposed on Amazonian mantle material surrounding north polar terrain [7]. While the crater is circular, rim height is not uniform around its circumference (Figs. 1-3). The rim is highest in the northeast (-3.4 km) and lowest in the west (-4.2 km). The lowest elevation of exposed floor is in the southwest (-6.2 km) (Fig. 1). The smooth-surfaced, roughly circular fill

deposit within Korolev does not extend completely to the interior walls of the crater, leaving an intervening ring-shaped trough (Figs. 1-3). Relative to the crater's center, the fill deposit is displaced to the north and east (Fig. 1), where it reaches closer to and higher up the crater walls (Figs. 2, 3). The highest point of the fill deposit (-4.7 km, roughly equivalent to the surrounding plains) is also displaced in the same sense (Figs. 1-3). The rim-to-floor depth expected at a fresh, unfilled crater of Korolev's diameter based on morphometric relations of martian craters is 2.3 km [15] to 2.9 km [16]. This range corresponds well with the observed range of maximum and minimum rim-to-floor depths (2.8 km and 2.0 km) using the floor elevation of the greatest exposed depth and the maximum and minimum rim elevations. This consistency in observed and predicted fresh depths suggests that the actual deepest point of the crater is not much deeper than the observed elevation, -6.2 km. The maximum thickness of the fill mound is then ~1.5 km [16].

Circum-South Polar Craters: There are many craters with fully or partially visible rims within the polar layered terrain of the south polar cap, especially on the half oriented towards 180° (e.g., Fig. 4). Around the fringes of the cap, northern parts of crater rims are fully exposed, while on pole-ward sides crater fill material is still clearly contiguous with polar material (e.g., Fig. 5). Up to ~12° of latitude from the edge of the polar layered terrain are craters with fill material isolated from polar material (e.g., Fig. 6). This isolated fill appears to become less circular and symmetric at greater distances, often located in the northern portions of the crater (e.g., Fig. 7). These materials have been mapped as extensions of polar layered material (Apl [7]) or as ice and fine dune material possibly derived from polar layered terrain and possibly covering polar layered terrain material deposited in areas of low wind velocity (Ad [7]).

Based on morphologic and topographic similarity, and in some cases contiguousness, with polar layered deposits, it seems likely that fill material may be of the same composition, possibly deposited by the same process. In this scenario, fill material was either 1) deposited preferentially in craters rather than on surrounding plains, or 2) once present in the plains as well, as part of a larger polar cap, and preferentially remains in the craters as polar material has retreated from the plains. Fill material in craters partially visible around the edges of the polar layered terrain appears to be maintained by the same conditions maintaining the surrounding, extra-crater polar layered terrain, unless both materials are being deflated and the craters are being exhumed. In some cases there is evidence that physical flow of polar layered material contributed to crater fill deposits [8]. Further north, craters not physically connected to the polar layered terrain contain less fill, which is generally in the form of a circular mound. Yet further north, crater fill is significantly less, occur-

ring only locally within craters. The observed trend of decreasing fill amount with increasing northerly latitude suggests that either deposition and equilibrium-amounts of fill are less at more northern latitudes, or erosive, sublimation, or ablation processes have been more severe at more northern latitudes.

To constrain the formation and modification of this fill material, we examine the radiative geometries and properties unique to the crater interior environment that may cause local energy balances to favor the presence of volatile-rich fill material in the craters over the plains. To consider the hypothesis of preferential deposition, we examine the concept of craters as cold traps, noting that this should not be assumed as the shadowing effects of crater walls are minimal at the centers of large craters. To consider the hypothesis of remnant volatile-rich material being left behind by a retreating ice cap, we again compare the stability of ice in the plains with that in a crater, but we also investigate whether geometry and insolation asymmetries expected from modeling energy-driven sublimation processes can account for the observed asymmetries in crater fill shape. As a proxy for evolution of the modification process, we use characteristic fill morphologies at increasing distance from the polar cap terrain. If shape is largely consistent with these modeled processes, then the deposit is likely largely ice-rich, and radiative effects may dominate over wind effects in the size, location, and shape of such crater fill.

Energy Balance Model: Our approach to determine where and how much modification of an assumed existing water-ice crater-fill occurs is to calculate the main energy input and output pathways for a patch of the surface and assume any excess input energy is available for sublimation. The main processes involved are as follows: 1) solar insolation, incremented by 5 minute intervals over a martian year, including the slope and slope direction of the surface and the shadowing effects of the crater walls, 2) temperature-dependent re-radiation from the surface, including the geometric effects of the crater walls on reducing emittance to the sky, 3) diffusion of heat into or out of the body of ice below the surface, and 4) energy, if any, available for phase change and sublimation [17]. By iteratively calculating the energy balance of these processes at different points within the crater, we can determine the relative amount of sublimation at each point.

In this investigation, we are interested in timescales less than those of eccentricity and obliquity variations, given the rapid rates of sublimation expected on Mars [13], so we hold orbital parameters constant. The sensitivity of the model and resulting crater-fill morphology and asymmetry is assessed with respect to physical and geometric parameters such as albedo, emissivity, slope angle, atmospheric scattering (based on [18]), proximity to the crater wall, crater wall height, subsur-

face percent ice (and associated dependence on conductivity, heat capacity, and density).

The relative role of incident solar radiation on differently-facing slopes is dramatic. As expected at the high northern latitude of Korolev, south facing slopes receive more total yearly insolation, yet the maximum daily insolation occurs on north-facing slopes due to obliquity effects. With a nominal, non-dust storm, atmospheric optical depth of 0.5, incident insolation is reduced by 10-30% when the sun is more than 10° above the horizon [18]. Albedo can vary by a factor of 4 [17], which directly effects absorbed insolation. The latter two effects affect the total amount of insolation, while the first, and the geometry of the crater, affect the relative distribution of insolation. Asymmetry in insolation is clearly a candidate for being the major control on volatile fill asymmetry. This is supported by observation in a north-south profile across Korolev (Fig. 2) showing a strong asymmetry in which fill is concentrated to the north, consistent with more yearly energy input from southerly insolation.

However, because insolation from the west and east are similar, it is evident from the asymmetry in an east-west profile of Korolev fill (Fig. 3) that other factors are influencing fill morphology. In this case, a strong east-west asymmetry in rim height (Fig. 3) suggests that shadowing by a high rim may be a secondary, or possibly locally primary, influence on volatile fill stability.

A nearby high rim, however, will also decrease radiative heat loss by reducing the angle of sky seen by a surface [17]. Due to a thin atmosphere that is ineffective at convecting heat, the sky on Mars is very cold relative to these crater walls. Thus, the greater the visible angle of sky, the more energy can be radiated away, and the more the crater wall fills the field of view, the less the effective emissivity [17]. This concept of effective emissivity is summarized in the following equation: *radiated energy* = :

$$(E\epsilon T_{surf}^4 - \epsilon T_{sky}^4) * skyfraction + (E\epsilon T_{surf}^4 - \epsilon T_{cwall}^4) * cwallfraction \quad (1)$$

where E is emissivity of the surface, ϵ is the Stephan-Boltzman constant, and T is the temperature of the surface, sky, and crater wall, respectively. The hemisphere centered on the normal to the surface is divided into that fraction which is open to the sky and that which is filled, or “blocked” by the crater wall.

Conduction of energy into the subsurface is represented very simply by a one-layer slab the thickness of the skin depth. It is assumed that, at each iteration of time, this slab changes temperature based on its heat capacity and the difference between its temperature at the previous time iteration and the temperature at the surface.

Future Application: While absolute amounts of sublimation may be attainable in the future, we are currently mainly interested in what factors control the asymmetry of the deposits, for which relative differences around the crater are sufficient. By modeling Korolev with both a uniform rim and a more realistic approximation of varying rim height, the role of rim height in combination with azimuth orientation of fill material slope will be assessed. By applying the model to circum-south polar craters, we will test the hypothesis that observed latitudinal trends in fill material morphology result from modification by radiative processes of remnants of a retreated polar cap.

References: [1] Scott, D. H., and K. L. Tanaka (1982) *JGR* 87, 1179-1190. [2] Schutlz, P. H., and A. B. Lutz (1988) *Icarus* 73, 91-141. [3] Forsythe, R. D., and J. R. Zimelman (1989) *Nature* 336, 143-146. [4] Head, J. W. (2001) *LPSC XXXII*, Abstract #1394. [5] Hynek, B. M. et al. (2002) *LPSC XXXIII*, Abstract #1408. [6] Malin, M. C., and K. S. Edgett (2000) *Science* 290, 1927-1937. [7] Tanaka, K. L., and D. H. Scott (1987) USGS Map I-1802-C. [8] Head, J. W. (2001) *JGR* 106, 10,075-10,085. [9] Fishbaugh, K. E., and J. W. Head (2000) *JGR* 105, 22,455-22,486. [10] Russell, P. S., and J. W. Head (2002) *GRL* 29, 17, doi:10.1029/2002GL015178. [11] Russell, P. S., and J. W. Head (2002) *Eos Trans. AGU Suppl.* F849. [12] Clifford, S. M. (1993) *JGR* 98, 10,973-11,016. [13] Kreslavsky, M. A., and J. W. Head (2002) *JGR* 107, E12, doi:10.1029/2001JE001831. [14] Head, J. W. et al. (2002) *Microsymposium* 36, Abstract #MS031, Moscow, Russia. [15] Pike, R. J. (1988) in *Mercury*, F. Vilas et al., eds., Univ. Arizona Press, 165-273. [16] Garvin, J. B. et al. (2000) *Icarus* 144, 329-352. [17] Hecht, M. H. (2002) *Icarus* 156, 373-386. [18] Pollack, J. B. et al. (1990) *JGR* 95, 1447-1473.

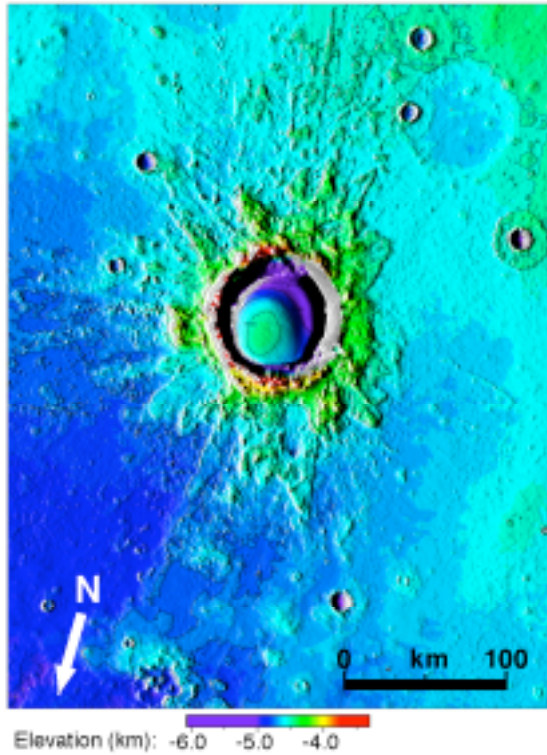


Figure 1. Gridded MOLA topography of Korolev Crater.

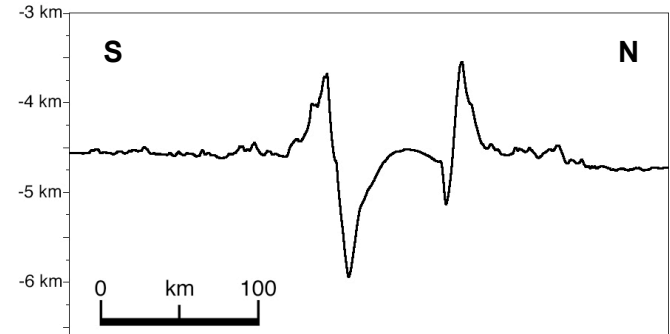


Figure 2. South-north altimetric profile of Korolev Crater.

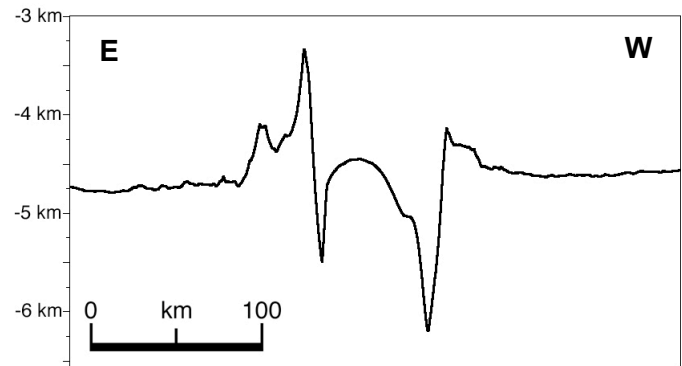


Figure 3. East-west altimetric profile of Korolev Crater.

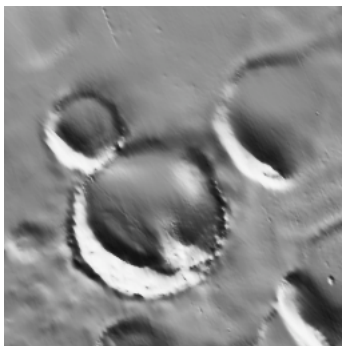


Figure 4. Crater rims visible, or partially visible, through the south polar layered terrain. Main crater is 100 km wide, at 75°S, 120°W. All images at roughly the same scale.

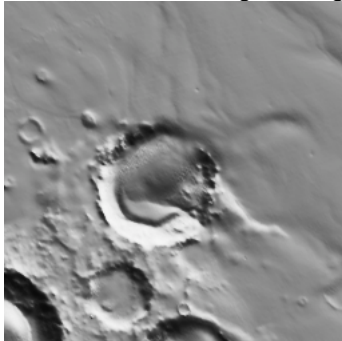


Figure 5. Crater mostly exposed, but still half surrounded with south polar layered terrain. Fill material is still contiguous with polar terrain. Crater is 55 km wide, at 80°S, 124°W.

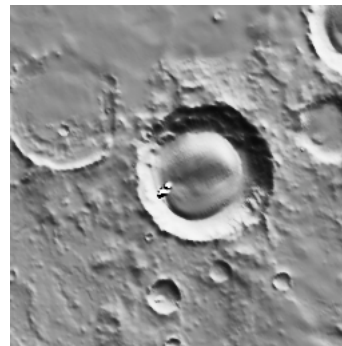


Figure 6. Crater isolated from south polar layered terrain, with circular fill material. Nearby fringes of polar layered terrain visible at top. Crater is 70 km wide, at 78°S, 126°W.

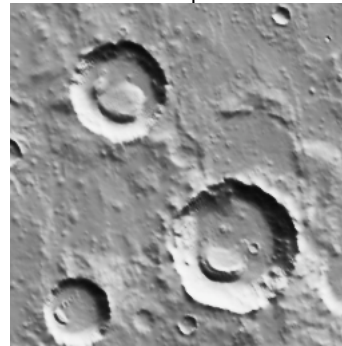


Figure 7. Craters with local, isolated, irregularly-shaped fill material. These craters are furthest from the polar layered terrain. Large crater is 50 km wide, at 74°S, 131°W.